8

Planetary structural mapping

Kenneth L. Tanaka
U.S. Geological Survey, Flagstaff

Robert Anderson
Jet Propulsion Laboratory, California Institute of Technology, Pasadena

James M. Dohm
Department of Hydrology and Water Resources, University of Arizona, Tucson

Vicki L. Hansen
Department of Geological Sciences, University of Minnesota Duluth

George E. McGill
University of Massachusetts, Amherst

Robert T. Pappalardo
Jet Propulsion Laboratory, California Institute of Technology, Pasadena

Richard A. Schultz
Geomechanics – Rock Fracture Group, Department of Geological Sciences and Engineering, University of Nevada, Reno

and

Thomas R. Watters
Center for Earth and Planetary Studies, National Air and Space Museum, Smithsonian Institution, Washington, DC

Summary

As on Earth, other solid-surfaced planetary bodies in the solar system display landforms produced by tectonic activity, such as faults, folds, and fractures. These features are resolved in spacecraft observations directly or with techniques that extract topographic information from a diverse suite of data types, including radar

Planetary Tectonics, edited by Thomas R. Watters and Richard A. Schultz. Published by Cambridge University Press.

backscatter and altimetry, visible and near-infrared images, and laser altimetry. Each dataset and technique has its strengths and limitations that govern how to optimally utilize and properly interpret the data and what sizes and aspects of features can be recognized. The ability to identify, discriminate, and map tectonic features also depends on the uniqueness of their form, on the morphologic complexity of the terrain in which the structures occur, and on obscuration of the features by erosion and burial processes. Geologic mapping of tectonic structures is valuable for interpretation of the surface strains and of the geologic histories associated with their formation, leading to possible clues about: (1) the types or sources of stress related to their formation, (2) the mechanical properties of the materials in which they formed, and (3) the evolution of the body's surface and interior where timing relationships can be determined. Formal mapping of tectonic structures has been performed and/or is in progress for Earth's Moon, the planets Mars, Mercury, and Venus, and the satellites of Jupiter (Callisto, Ganymede, Europa, and Io). Structures have also been recognized on some of the Saturnian (Titan, Dione, Rhea, Tethys, Iapetus, and Enceladus) and Uranian satellites (Miranda and Ariel) and Neptune's large moon, Triton. Of these, only Earth's Moon has provided rock samples that have been dated using radiometric techniques, thus constraining, in the best scenarios, the age of formation of specific structures. However, most of these bodies have a resurfacing history useful for relative structural history, which might be constrained by geologic mapping and, in some cases, by crater-density data. Because of the range in rheologic character represented by planetary crustal materials and in some cases exotic stress mechanisms acting upon them, planetary structures can include forms, relationships, and developmental patterns that are rare or non-existent on Earth.

1. Introduction

Structural mapping constitutes the fundamental approach to documenting the tectonic deformation of planetary surfaces in space and time. As on Earth, geologists characterize, map, and interpret rock materials and structures on planetary surfaces to interpret geologic histories from local to global scales. However, terrestrial mapping approaches need to be adapted to meet the needs and special challenges inherent in producing planetary geologic maps that rely on spacecraft data and lack ground truth. The philosophical basis and basic techniques used for all current planetary geologic mapping were developed by geologists studying the Moon prior to, during, and following lunar exploration using space vehicles. In particular, mappable units were defined by objective descriptive criteria that do not depend on genetic interpretations. Crustal history was determined by means of superposition and crosscutting relations, and by density of superposed craters. Wilhelms

(1972, 1990) provides a thorough exposition of this approach. Structures, especially craters, provide critical elements to this stratigraphic approach. Adequate data for mapping structures on a variety of planetary bodies have increased dramatically over the past few decades and now are available for Earth's Moon, Mercury, Mars, Venus, and the satellites of Jupiter, Saturn, and Neptune, as well as the asteroid Eros.

Tectonic structures result from deformation of crustal rock materials and may include individual or systems of joints, faults, folds, and combinations thereof in various size ranges (see Schultz *et al.*, Chapter 10). Such structures are expressed at the surface by a diversity of landforms that combine the morphology of the pre-deformed surface with that of the tectonic deformation. In addition, subsequent modification due to erosion, burial, and reactivation of deformation modifies the appearance of structural landforms. Morphology can be observed using suitable bases constructed from visible, infrared, and radar imaging data, as well as digital elevation models derived from laser altimetry, stereo photogrammetry and 2-D photoclinometry. Except in limited cases where good exposures and topographic information permit accurate measurement of stratigraphic offsets, the nature of deformation is inferred from a comparison between the planetary landform and the geologist's knowledge of Earth-based examples. Brittle extensional structures appear in spacecraft imagery as linear topographic elements with negative and/or positive relief, including normal faults, grabens, and rift systems that cut and commonly produce offsets in the strata (e.g., McGill, 1971; Wilhelms, 1987; Banerdt *et al.*, 1992; Schultz, 1991, 1999). Contractional structures, on the other hand, might be expressed as positive relief landforms, such as wrinkle ridges that overlie blind thrust faults (that do not break the planetary surface; e.g., Schultz, 2000a), surface-breaking thrust faults expressed by lobate scarps (see Watters and Nimmo, Chapter 2; Golombek and Phillips, Chapter 5), high-angle reverse faults expressed by high-relief ridges (see Watters and Nimmo, Chapter 2) and large mountain ranges that often mark the locations of buckled and/or over-thrusted crustal materials (e.g., Banerdt *et al.*, 1992; Schultz and Tanaka, 1994; Dohm and Tanaka, 1999; Schultz, 2000a). Strike-slip faults are found on several planets and satellites and display evidence of either brittle or ductile deformation, or both (e.g., Koenig and Aydin, 1998; Schultz, 1989, 1999; Watters, 1992; Schenk and McKinnon, 1989; Pappalardo *et al.*, 1999; Tuckwell and Ghail, 2003; Kumar, 2005; Okubo and Schultz, 2006).

Structural history is reconstructed among structures and materials such as lava flows, impact ejecta, and sedimentary deposits through crosscutting relations determined using all pertinent spacecraft information. This Earth-proven technique requires meticulous detective work. The spatial and temporal associations of tectonic structures among rock materials archive past geologic events, which can be

thoughtfully deciphered through detailed geologic mapping. However, actual geologic histories are typically much more detailed and complex than can be fully realized and represented on a geologic map, and age correlations are commonly poorly constrained.

As with any archive of past events, evidence can be destroyed or buried. Therefore, mappers effectively reconstruct structural histories based on (1) collecting and synthesizing all available data and compiled geologic information, (2) clearly discussing applied methodologies and acknowledging critical assumptions and uncertainties, and (3) avoiding overinterpretation and bias. Geologic mapping, whether based on field investigations or remotely sensed data, is ultimately built on consistency arguments. Thus mappers' observations, assumptions, and interpretations should always be open to further scrutiny, including how interpretations imply relations about other units, structures, and history (e.g., Gilbert, 1886).

Absolute-age determinations, which depend on sizable returned samples, are only directly available for six locales on the Moon (e.g., Wilhelms, 1987). However, crater-density statistics are useful relative-age indicators for the more heavily cratered planetary bodies, because impact cratering is assumed to be a continuing, areally random process for most surfaces. The number of craters superposed on a surface provides an average relative age of the surface. For example, the density of superposed craters on the lunar highlands is much greater than the density of superposed craters on the lunar maria. If the flux of impacting objects was constant through time, an unrealistically young age for the maria and for post-mare craters is implied. Thus, it was realized that the flux was greater by orders of magnitude early in lunar (and solar system) history than in more recent time. Returned samples verified this inference. A controversy still exists, however, with regard to the nature and rate of the bolide flux decline. The radiometric ages of lunar basin ejecta seem to imply that most basin impacts occurred during a relatively brief interval of time, with essentially no surface ages older than about 4.1 Ga and none younger than about 3.8 Ga, with a major spike of impact events at about 3.9 Ga (Tera *et al.*, 1974; Kring and Cohen, 2002; Gomes *et al.*, 2005; Strom *et al.*, 2005). This "cataclysmic" model implies a very different history of the Moon during its first few hundred million years of existence than does the alternate model, which postulates a continuous, exponential decline in impact flux with time. The absence of direct evidence of basin events older than about 4.1 Ga may be due to complete destruction of evidence for older basins, including radiometric dates demonstrating associated basin-related activity, or to incomplete sampling dictated by the logistical constraints on the Apollo missions. Absolute ages for non-lunar planetary surfaces can be estimated, or modeled, based on extrapolations of impactor populations, cratering theory, the cratering-rate history determined for the Moon, and

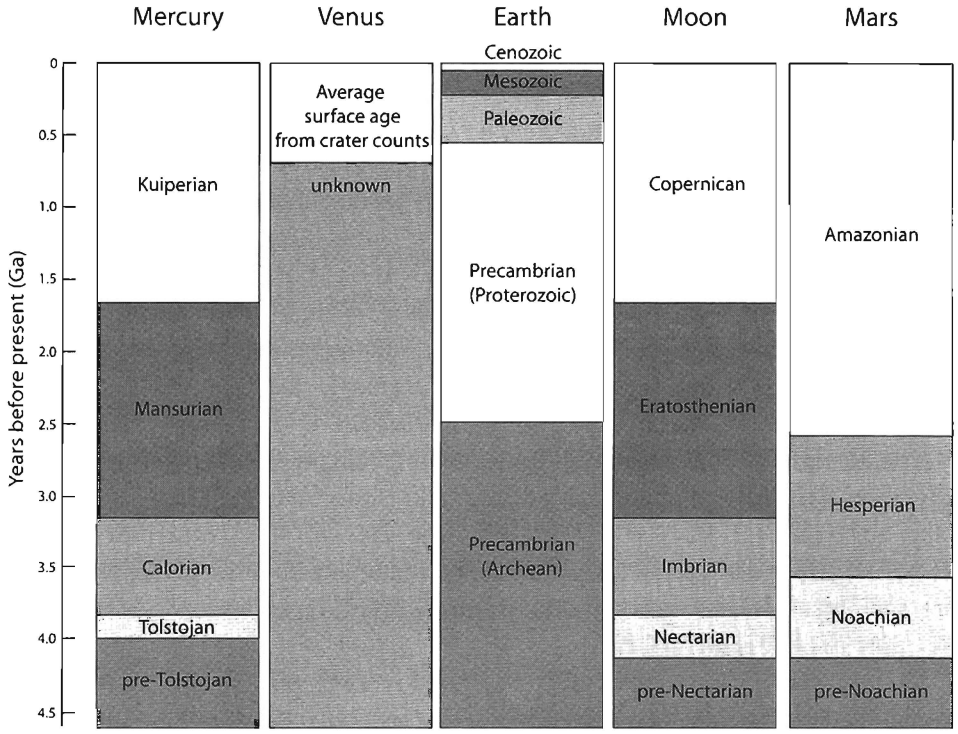

Figure 8.1. Geologic timescales for bodies of the inner solar system (after Tanaka and Hartmann, 2008).

other effects related to orbital distance from the Sun (e.g., Hartmann and Neukum, 2001). Based on this approach, absolute ages (having various degrees of uncertainty) for geologic epochs on the inner planets of the solar system are shown in Figure 8.1.

Maps that delineate structures of various ages can be used to characterize potential stress sources, strain magnitudes and history, and preexisting structural controls that may relate to episodes of local to global volcanism, tectonism, and impact cratering. Evidence for tectonic strain includes deformed features such as impact craters, which may hint at the type and amount of tectonism in the region or at the rheological nature of the impacted material, through assessing their geometric shape (Golombek *et al.*, 1996; Pappalardo and Collins, 2005). Tectonic structures and deformational processes may also control subsequent volcanic, intrusive, and hydrogeologic activity, including the diversion of surface and subsurface lavas and volatiles, as well as the discharge of subsurface fluids. Such activity can result in structurally controlled drainage pathways and canyon systems, aligned collapse features (e.g., pit crater chains), and volcanic constructs. Other indirect

evidence for tectonism includes aligned mesas and valleys, such as those located in and surrounding large impact basins, where valleys and mesas radial to and concentric about the basins imply impact-related deformation of crustal materials (e.g., Melosh, 1989). Detection of major structures whose original landforms are all but destroyed by erosion may be indicated through structurally controlled linear anomalies in gravity, magnetic, mineralogic, geochemical, and other data (e.g., Dohm *et al.*, 2007b).

Structural landforms are schematically shown on geologic maps through line symbols. Sometimes the lines are dashed, dotted, or queried to indicate that they are buried or have an uncertain designation. Additional symbols and colors are used to denote structure type, sense of displacement, and age. At times, closely spaced sets of structures are indicated by stipple patterns. In more recent mapping efforts, tectonic structures are digitized, enabling comparative analysis of tectonic structures in time and space using Geographic Information Systems (GIS) and other software (Tanaka *et al.*, 1998; Dohm and Tanaka, 1999). Structure densities and orientations and spatial associations of structures with other geologic features are examples of what can be produced through GIS-based analysis of structural mapping (Dohm *et al.*, 2001a).

Overall, planetary structural mapping provides unique insights into the deformational histories of planetary bodies. Structural mapping is integral to determining geologic histories at global to local scales, to evaluating geophysical, geochemical, and even in some cases climatic models relating to the time–space relations of the planet's interior, surface, and atmosphere (if present), to constraining surface rheology at various scales and through time, and to planning science objectives and designing experimental approaches for future planetary missions (e.g., Schulze-Makuch *et al.*, 2007; Furfaro *et al.*, 2007).

2 Mapping and dating structures with spacecraft data

2.1 Mapping with visible and infrared images

Images of planetary surfaces in visible and infrared wavelengths of adequate spatial resolution permit mapping and interpretation of surface landforms resulting from structural deformation (e.g., Avery and Berlin, 1992; Golombek, 1992; Lillesand and Kiefer, 1994; Bell *et al.*, 1999). Data characteristics and quality are governed by planetary characteristics and the characteristics of the spacecraft camera systems. Following Lunar Orbiter photographs recorded on film in 1966–1967, Mariner, Viking, and Voyager spacecraft missions to Mars, Mercury, and the outer planetary satellites employed vidicon cameras that obtained digital images sensitive to light in the 350 to 650 nm wavelength range, with filter wheels

providing broadband multi-spectral color imaging. Later, charge-coupled device (CCD) cameras, which expanded the sensitivity range to include near-ultraviolet to near-infrared wavelengths (200 to 1100 nm), have been used for missions to Mars, the Moon, the satellites of Jupiter, and asteroids (Mars Global Surveyor, Mars Odyssey, Mars Express, Clementine, Galileo, Giotto, and Near-Earth Asteroid Rendezvous).

Digital images are compiled as two-dimensional grids (i.e., raster arrays) composed of individual, square picture elements ("pixels"). Surface brightness is governed by the albedo of the surface (the ratio of reflected to incident surface energy within a defined wavelength range) and by illumination and surface geometries. Clouds can have a substantial albedo, thereby obscuring the underlying surface of planets with atmospheres. Images may be acquired in various geometries and illumination conditions. Some images, such as obtained by the Mars Orbiter Camera (MOC) and Thermal Emission Imaging System (THEMIS), primarily involved nadir (vertical) pointing of the camera, whereas other camera systems used extensive off-nadir pointing. Imaging campaigns that collect data at different seasons and times of day across the curving planetary surface capture variable directions of solar illumination and local surface changes. For Mars, seasonal haze and transient dust and CO_2 clouds may obscure surface viewing.

Higher resolution images provide correspondingly smaller areal coverage. In order to coherently map broad surfaces at highest resolutions, multiple images are combined into mosaics. Because lighting and atmospheric conditions and camera location, pointing, and color filter vary, photometric and geometric corrections are required. Spacecraft jitter and location uncertainties and camera noise effects also call for cosmetic improvements. However, some of these effects cannot be completely corrected through image processing techniques; for example, morning and afternoon lighting conditions will result in the reversal of hill-slope shading, which can result in confusing image mosaics. The more serious effects need to be recognized and documented to avoid mistaking them for surface features. In addition, geodetic control of the positioning of landforms varies according to available data and modeling. Thus, the mapped locations might include significant errors. This problem is especially evident in areas where the controls do not permit proper alignment of features between adjacent images in a mosaic.

Given the aforementioned limitations to image data, morphologic analysis can be performed where slope information can be gleaned. Both visual and thermal infrared images include intensity variations related to slope orientation vs. incident solar illumination, where sunlit slopes tend to be relatively bright (or warm in thermal infrared) and shaded (or cool) slopes tend to be dark. In addition, albedo variations of surface materials may highlight tectonic structures (e.g., structurally controlled deposits).

2.2 Mapping with radar images

Radar, radio detection and ranging – a form of active (i.e., it provides its own energy source) remote sensing – is able to operate generally independent of solar illumination or weather conditions. With the correct wavelength, radar "sees" through clouds or other media that might obstruct energy in visible light and other wavelengths. Radar works within the microwave band of the electromagnetic spectrum in the wavelength range from millimeters to 100 cm. Radar illuminates a terrain, detects return energy (radar return), and records an image. Three factors affect radar return: terrain slope (topography), terrain roughness (at the scale of the radar wavelength), and terrain electrical properties. The third factor, a function of composition and/or bulk density, is the hardest to quantify; we consider the first two in our brief discussion.

The military developed radar-imaging techniques in the 1950s. Geological applications began with image system declassification in the mid-to-late 1960s, and advanced in the 1970s with commercial radar image availability. Radar image analysis is largely similar to visible and infrared image analysis and primarily comprises "photogeologic" investigation of primary and secondary structures marked by topography or surface roughness. As such, geologic history interpretation must follow similar cautions (e.g., Hansen, 2000). Radar data are particularly useful for recognizing promontories or geomorphic features and linear ridges or troughs that represent fractures, faults, and folds as confirmed by field mapping. Radar data, acquired by orbiting spacecraft, can contribute to geological analysis of any solid planet surface. For example, NASA Magellan radar returned global coverage of breathtakingly detailed images of Venus' cloud-covered surface that form the basis of our understanding of Venus' tectonic and magmatic evolution (e.g., Solomon *et al.*, 1992; Ford *et al.*, 1993).

Although radar images resemble black-and-white photographs, radar's side-looking system requires a few simple considerations in interpretation. Oblique radar illumination produces strong signal returns and peaks that highlight surface roughness, which includes topographic highs (positive features), such as ridges, scarps, and promontories, and lows (negative features), which may include pits and impact craters, depending on shape, size (at radar resolution), and orientation with respect to radar illumination. Structures recognizable by their resulting landforms in radar images include: folds, grabens, faults, fractures, volcanic edifices and summit craters, impact craters, collapse depressions, and valley features such as Venusian valley networks (Komatsu *et al.*, 2001). Ground range images, a function of illumination direction and incidence angle and slope, form 2-D representations of 3-D surfaces. Radar artifacts, including radar shadow, foreshortening, and layover, can deter topographic interpretation or add geometric clues absent

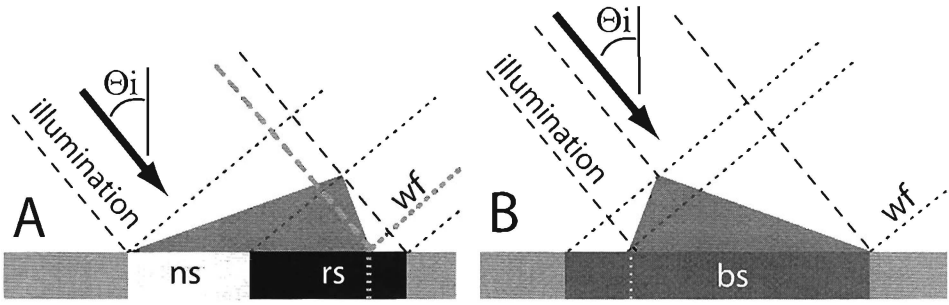

Figure 8.2. Radar ground-range images (basal strip) resulting from different topographic form, incidence angle (Θ_i), and illumination direction. Points on topographic form project parallel to wavefront (wf, perpendicular to illumination) to points on the ground-range image. Projected location and size of near slope (ns), back slope (bs) and radar shadow (rs) shown with shades of gray indicative of relative radar return and hence brightness. Gray lines show where surface locations would not be imaged. (A) Left illumination of asymmetric topographic form; foreshortening and radar shadow result in apparent symmetric shape. The point at the base of the near slope "projects" to its correct location; the high point projects forward of its true location; the base of the far slope "projects" to its correct location, but its presence is lost in radar shadow. The shallow near slope is imaged (ns), but it is "foreshortened" in the ground-range image; the entire far (steep) slope is lost in radar shadow. (B) Left illumination and an asymmetric topographic form with steep slope facing radar results in extreme foreshortening (called "layover"). Only the far slope is imaged because the high point projects forward, and the sharp break in slope is lost in extreme foreshortening, or layover. Although the near slope is lost to layover, none of the far slope is lost to radar shadow in this case.

in plan view imagery (Figure 8.2). Sharp breaks in slopes result in sharp changes in radar brightness in the ground range image, whereas gradual changes in slope yield gradual changes in radar brightness. Radar shadow, similar to visible light side-illumination shadowing, can hide breaks in slope. Foreshortening shortens the near slope or the slope facing radar illumination (Figure 8.2a). Layover, an extreme form of foreshortening, shortens the radar-facing slope so much that it disappears on the ground-range image, and only the back slope appears in the image (Figure 8.2b). Attention to radar illumination and wave-front geometry should yield consistent topographic interpretation among analysts, although geological interpretations of topography might be debated. Interpretation of material boundaries in radar imagery can be more controversial because radar backscatter could result from surface roughness (such as a pahoehoe flow versus aa flow surface) or from terrain electrical properties, or both. In addition, a single volcanic flow might change from pahoehoe to aa character resulting in a variable surface roughness that could yield a wavelength-dependent radar signature; yet the flow could have

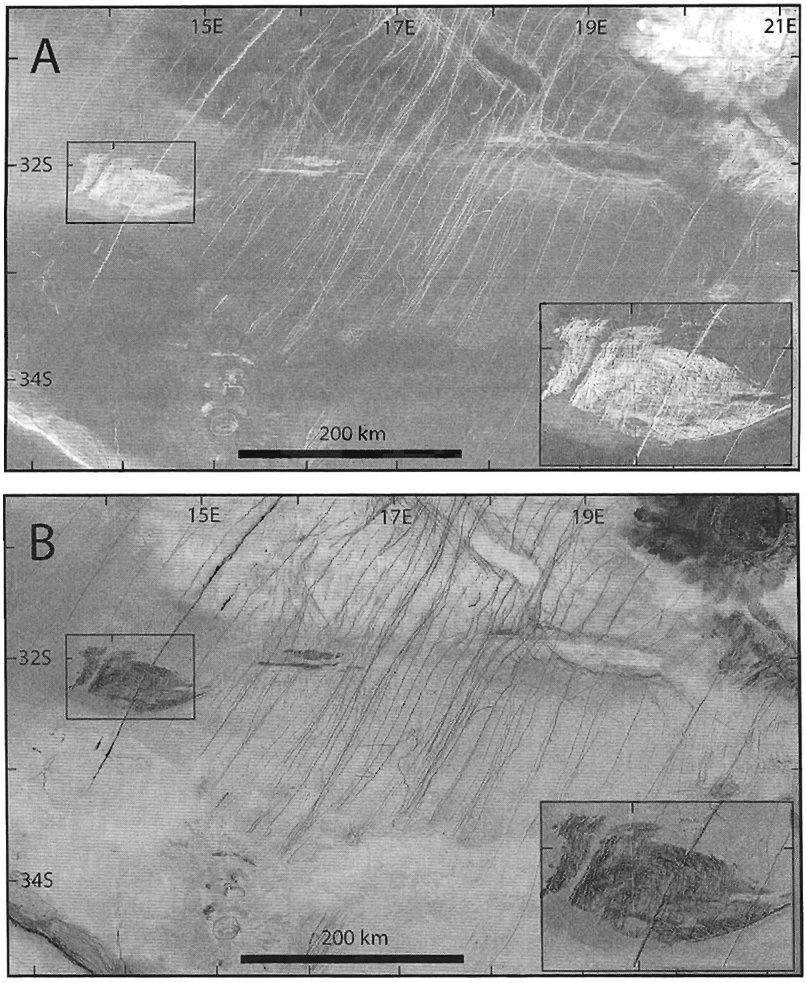

Figure 8.3. Comparison of left illumination SAR (A) and inverted SAR (B). Note impact crater in northeast corner of images and volcanic construct and northwest-trending fold belt in southwest corner. North–northeast trending fractures and pit chains are truncated. and thus post-dated, by flows in the southern sector. Insets show ribbon tessera terrain with west–northwest trending folds and north–northeast trending ribbon structures.

been emplaced as a single temporally equivalent geological unit. Thus, it is critical to consider radar interpretation separate from geological interpretation. Ford *et al.* (1993) provide an excellent review of radar interpretation with particular emphasis on Venus Magellan data.

Radar is exceptionally well suited for the identification of primary (emplacement related) or secondary (tectonic) structures that comprise 3-D topographic expression, while providing local to regional synoptic views of fracture, fault, and lineament patterns. Given that many secondary structures form lineaments, inverted or negative radar imagery commonly illustrates features more clearly because the human eye more easily differentiates dark lines on bright backgrounds rather than bright lines on dark backgrounds (Figure 8.3). Paired radar images with different incidence angles can be combined to construct stereo anaglyphs (e.g., Plaut, 1993),

or radar data and complementary altimeter data can be combined to make synthetic stereo anaglyphs (Kirk *et al.*, 1992). Such data have been used with great success in Venus mapping (e.g., Hansen *et al.*, 1999, 2000).

The interpretation of geologic structures, material units, temporal relations among the structures and material units, and ultimately the geologic history using radar requires the same careful consideration that should be employed with any remote sensing dataset (e.g., Wilhelms, 1972, 1990; Tanaka *et al.*, 1994; Hansen, 2000). Radar data permit effective mapping of surface morphologies and structures (e.g., Ford *et al.*, 1989, 1993; Sabins, 1997). Geologic unit boundaries are, in many cases, clearly defined by radar backscatter intensity, as well as by crosscutting relations among materials and positive and negative features. Gradational contacts, or contacts not marked by radar distinctive features, can be difficult to trace. Termination of tectonic structures may represent the spatial limit of a deformation front, or termination might indicate the limit of younger on-lapping material. Structural facies boundaries represent a strain discontinuity related to a tectonic process, perhaps marked by a decrease in structural element density; younger burial is more likely if structural elements are abruptly truncated at a high angle to structural trend.

2.3 Mapping with topography

Topographic data also provide critical clues for tectonic landform analysis. Topographic data are critical to the proper characterization of the morphology and structural relief of tectonic landforms, which is required to identify the structure, to provide estimates of strain, and to formulate and test kinematic and mechanical models of the candidate structures (e.g., Schultz and Zuber, 1994; Schultz, 2000a; Okubo and Schultz, 2004, 2006). In addition, topographic data have revealed the presence and spatial extent of structures that are not readily detected in images.

Topographic data for tectonic landforms have been derived from images using a number of techniques. The most basic of these is shadow measurements. High spatial resolution topographic data can be obtained from single images using quantitative modeling of slope variations, or photoclinometry (see Hapke *et al.*, 1975; Davis and Soderblom, 1984; Kirk *et al.*, 2003). On Mars, photoclinometry has been applied to Viking, MOC, and other images for landforms in areas or conditions where albedo variations are minimal; relative errors in this technique can be below 5% (Davis and Soderblom, 1984; Tanaka and Davis, 1988). Another important means of obtaining high-resolution topographic data is from stereo imaging. Using digital stereo methods that employ automated and semi-automated matching algorithms, it is possible to obtain DEMs with spatial resolution and height accuracy

limited only by the resolution and signal-to-noise ratio of the images (see Watters *et al.*, 1998; Cook *et al.*, 2000; Schenk and Bussey, 2004). These methods have also been used to derive topography from stereo radar images (see Herrick and Sharpton, 2000).

Topographic data for the terrestrial planets have also been obtained from Earth-based radar altimetry (see Downs *et al.*, 1982; Harmon *et al.*, 1986) and radar interferometry (Margot *et al.*, 1999). Radar interferometry compares two sets of radar altimetry data that yield differences in signal phase caused by elevation differences. Profiles derived from Earth-based radar altimetry have sufficient along-track spatial and vertical resolution to characterize individual tectonic features (see Watters and Nimmo, Chapter 2). These datasets provide regional context for more detailed topographic investigations of smaller-scale (local) structures, but have been largely superseded by measurement of planetary topography at regional and global scales by orbital spacecraft (such as for the Moon and Mars).

Global topographic data have been returned from radar and laser altimeters on orbiting spacecraft for Venus, the Moon, Mars, and asteroid 433 Eros (see Pettengill *et al.*, 1980; Ford and Pettengill, 1992; Zuber *et al.*, 1994; Smith *et al.*, 1999; Zuber *et al.*, 2000). For Venus and the Moon, current global topography datasets have high vertical but low spatial resolution. Although these data are important in determining the long-wavelength (i.e., regional) topography of deformed planetary surfaces, they generally lack the spatial resolution to resolve individual structural features. However, radar data can provide critical topographic constraints (e.g., Hansen, 2006). The Mars Orbiter Laser Altimeter (MOLA), in contrast, has returned some of the highest vertical and spatial (460 m to 115 m/pixel near the poles) resolution interpolated digital elevation models for any of the terrestrial planets thus far (Smith *et al.*, 1999, 2001; Zuber *et al.*, 2000; Okubo *et al.*, 2004). The high-resolution MOLA data were used to study Martian tectonic structures in unprecedented detail (e.g., Golombek *et al.*, 2001; Schultz and Lin, 2001; Schultz and Watters, 2001; Wilkins and Schultz, 2003; Okubo and Schultz, 2003, 2004, 2006; Schultz *et al.*, 2006; Golombek and Phillips, Chapter 4). These data have also revealed a previously undetected population of subdued wrinkle ridges in the northern lowlands of Mars, partly buried by sedimentary material (Withers and Neumann, 2001; Head *et al.*, 2002) or formed in weak materials (Tanaka *et al.*, 2003).

One of the challenges to mapping tectonic features using images and image mosaics is illumination bias introduced by the lighting geometry. Low-relief features in particular can be easily missed if the illumination direction is not favorable. Shaded-relief maps generated from DEMs with sufficient vertical and spatial resolution can be used to overcome illumination bias, because any illumination direction can be specified (Plate 23).

3 Structure mapping of planetary bodies

3.1 Moon

Important structures on Earth's Moon fall into three categories: impact craters, wrinkle ridges, and grabens (formerly called straight rilles; e.g., McGill, 1971; Masursky *et al.*, 1978; Golombek, 1979). Most of the extensional and contractional structures formed on the Moon were produced in association with impact basins (multiringed structures >300 km diameter on the Moon; e.g., Melosh, 1976, 1978, 1989; Solomon and Head, 1979, 1980; Golombek and McGill, 1983; Watters and Johnson, Chapter 4). Because of this relationship, wrinkle ridges and grabens received much attention in the earliest planetary structural mapping efforts (e.g., Schultz, 1976; Masursky *et al.*, 1978).

Until recent decades most geologists did not consider impact cratering an important geologic process. Terrestrial geologic experience indicated that sub-circular craters surrounded by material derived from the crater were volcanoes, and thus almost all geologists initially inferred that lunar craters were also volcanic. A notable early exception was Gilbert (1893), who recognized the importance of impact cratering in the evolution of the lunar crust. He also argued that the history of the Moon could be deciphered using techniques that are philosophically similar to those used by geologists studying the history of Earth. A major breakthrough in understanding was provided by the work of Baldwin (1963), who established a quantitative morphological continuum from bomb craters to lunar craters. By the mid 1960s, planetary scientists, with a small number of exceptions, considered this issue settled. The increasing realization that impact craters are not rare on Earth, and the analysis of returned lunar samples, finally ended this controversy.

Widespread ejecta deposits from large multiringed basins provide us with a relative timescale through use of classical superposition relations – younger ejecta deposits rest on older ejecta deposits. The lunar time–rock classification system is primarily based on the stratigraphy of basin deposits (Shoemaker and Hackman, 1962; Wilhelms, 1987). The interiors of many large multiringed basins are filled with relatively smooth, low-albedo material (the lunar maria), leading in the past to the concept that lunar maria is impact melt related directly to basin formation (e.g., Urey, 1952). But stratigraphic and crater-density relations indicate that the lunar maria are significantly younger than the impact basins that contain them (Figure 8.4). Indeed, returned samples demonstrate that the time gap between formation of lunar basins and their flooding by maria material spans hundreds of millions of years (e.g., Wilhelms, 1987). Within this stratigraphic framework, the formational ages of grabens and wrinkle ridges can be constrained by crosscutting and burial relations to outcrops of highland and maria materials.

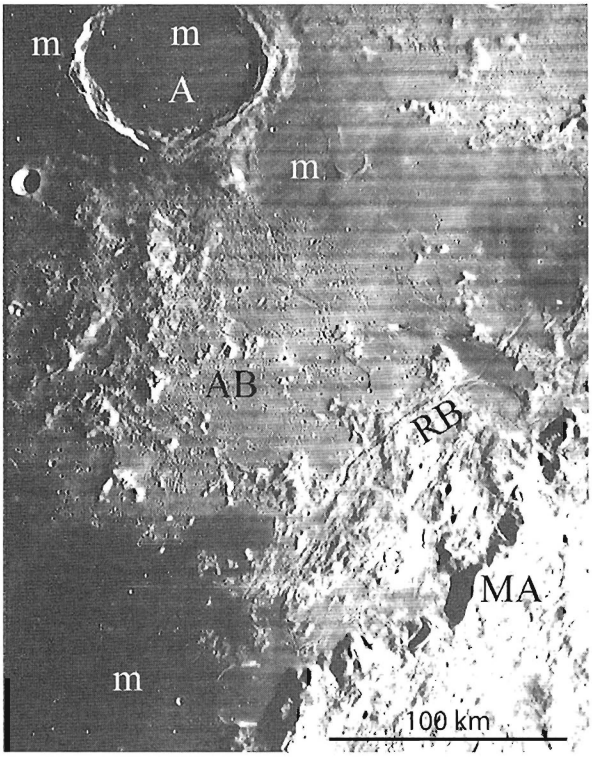

Figure 8.4. Southeastern margin of Mare Imbrium. Montes Apenninus (MA) is a portion of the Imbrian basin rim; all features interior to this rim must be younger than the basin impact event. AB, Apennine Bench Formation; m, mare basalts; A, crater Archimedes (83 km in diameter); RB, Rima Bradley, an arcuate rille (graben). The Apennine Bench Formation is interpreted to be the oldest post-impact material; Archimedes ejecta and secondary craters are superposed on it, and Rima Bradley cuts it. Archimedes crater and Rima Bradley are, in turn, superposed by dark mare basalts. This sequence demonstrates that the mare basalts cannot be directly due to the Imbrian impact event (Wilhelms, 1987). Lunar Orbiter image IV-109-H3; center at 13.8°N, 3.6°W; north toward top.

Lunar wrinkle ridges generally consist of a broad, low arch from a few to a few tens of kilometers across, surmounted by a narrower, sinuous ridge that may be either symmetrically or asymmetrically placed on the arch (Figure 8.5). Hypotheses for the origin of these landforms fall into two categories: magmatic or tectonic (e.g., Maxwell *et al.*, 1975). Abundant evidence from the Moon and other planets favors a tectonic origin, with wrinkle ridges representing anticlines formed as the lunar crust warped upward due to displacement on a subsurface thrust fault (e.g., Howard and Muehlberger, 1973; Maxwell *et al.*, 1975; Schultz, 1976; Lucchitta, 1976, 1977; Plescia and Golombek, 1986; Sharpton and Head, 1988; Watters, 1988; Golombek *et al.*, 1991; Schultz, 2000a). Most lunar wrinkle ridges occur in lunar maria, a likely testament to mechanical layering of deformed materials. Some wrinkle ridges appear to be due to differential compaction over buried crater or basin rims; others most likely formed as a result of basin floor subsidence following extrusion of lunar maria, and thus reflect folding and faulting of the maria material. The common presence of wrinkle ridges within basins indicates that basin subsidence and deformation followed maria emplacement.

Rilles form narrow troughs that range up to hundreds of kilometers in length. Two types of rilles occur: sinuous (Figure 8.5) and straight to arcuate (Figure 8.4). Sinuous rilles generally begin at pits or other putative volcanic features, and thus

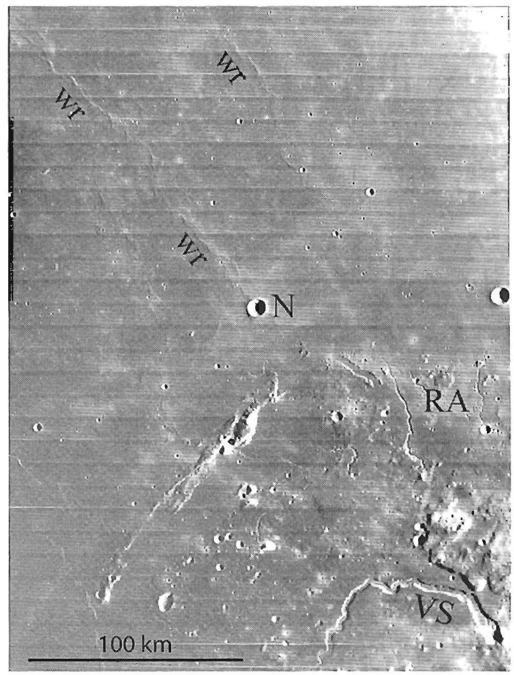

Figure 8.5. Interior of Oceanus Procellarum. Northwest of crater Nielsen (N) are typical wrinkle ridges (wr). The diameter of crater Nielsen is 10 km. Rimae Aristarchus (RA) and Vallis Schröteri (VS) are typical sinuous rilles, and are either collapsed lava tubes or lava channels. The material cut by the rilles, part of the Aristarchus plateau, is embayed by the younger mare basalts of Oceanus Procellarum. Lunar Orbiter image IV-158-H1; center at 42.0°N, 47.7°W; north toward top.

are believed to be analogous to terrestrial lava channels or collapsed lava tubes. The inferred volcanic source feature for a sinuous rille would be the same age as, or younger than, the materials crossed by the rille. Straight and arcuate rilles are grabens, as indicated by changes in rille width as it transects older topographic features, such as crater rims (McGill, 1971). These grabens commonly occur outside of and concentric to basins, and can be related to the same basin subsidence implied by intrabasin wrinkle ridges (e.g., Golombek and McGill, 1983). The three-dimensional geometry of straight and arcuate rilles has been used to estimate the thickness of the layer of impact ejecta (the megaregolith) that overlies local basement (Golombek, 1979; see Schultz *et al.*, 2007, for a recent reanalysis and discussion).

A less common lunar tectonic landform are thrust fault scarps (Lucchitta, 1976; Howard and Muehlberger, 1973; Binder, 1982; Binder and Gunga, 1985). These scarps are often lobate and segmented, analogous in morphology to planetary lobate scarps (Watters and Johnson, Chapter 4). In contrast to the lobate scarps on Mercury and Mars (see Watters and Nimmo, Chapter 2; Golombek and Phillips, Chapter 5), lunar lobate scarps are much smaller scale structures (Binder and Gunga, 1985; Watters and Johnson, Chapter 4). Although lobate scarps on Mercury and Mars can have over a kilometer of relief, lunar scarps have a maximum relief of much less than 100 meters (Lucchitta, 1976; Howard and Muehlberger, 1973; Binder, 1982; Binder and Gunga, 1985; Watters and Johnson, Chapter 4), indicating lower local

contractional strain accumulations. The lengths of the scarps are also small, with the longest segments reaching a maximum of only ~20 km (Binder and Gunga, 1985). In spite of their scale, lunar scarps are interpreted to be the result of thrust faulting (Lucchitta, 1976; Howard and Muehlberger, 1973; Binder, 1982; Binder and Gunga, 1985; Watters and Johnson, Chapter 4). Although the evidence of offset is not as dramatic as in the case of large-scale lobate scarps on Mercury and Mars, given the smaller surface gravity for the Moon that, in part, regulates the magnitude of fault offset (Schultz *et al.*, 2006), the morphology and the linkage between individual segments of the lunar scarps supports the interpretation that they are the surface expression of shallow thrust faults (Watters and Johnson, Chapter 4). The known lunar lobate scarps, as well as the mare ridges and grabens, have been mapped by Watters and Johnson (Chapter 4).

3.2 Mars

Although it has been more than 30 years since the Viking Orbiters imaged the surface of Mars, Mars' tectonic history continues to be a field of lively debate. Mars is dominated by two volcanic regions: the Tharsis magmatic complex of the western hemisphere (Dohm *et al.*, 2007a) and the Elysium rise of the eastern hemisphere (see Golombek and Phillips, Chapter 5). Large impact basins such as Utopia (McGill, 1989) and Hellas and the northern lowlands have also contributed to surface deformation. Tharsis is an enormous, high-standing region (roughly 25% of the surface area of the planet) capped by the solar system's largest shield volcanoes (e.g., Tanaka *et al.*, 1991; Banerdt *et al.*, 1992). This magmatic complex is the largest single tectonic and volcanic province on the terrestrial planets, with a rich history of geologic and tectonic activity that lasted throughout most of Martian geologic time (e.g., Solomon and Head, 1982; Dohm *et al.*, 2001b, 2007a; Phillips *et al.*, 2001).

As in the previous lunar work, stratigraphic mapping of regionally extensive terrains on Mars provides the context for defining the relative ages of major deformational events (e.g., Scott and Tanaka, 1986; Greeley and Guest, 1987; Tanaka, 1986, 1990; Tanaka *et al.*, 1991, 1992; Scott and Dohm, 1990, 1997; Dohm and Tanaka, 1999; Dohm *et al.*, 2001a,b; Anderson *et al.*, 2001; Knapmeyer *et al.*, 2006). In contrast to the Moon, however, internal processes have largely dominated the production of surface-breaking structures on Mars, with impact-basin tectonics playing a subsidiary role (e.g., Phillips *et al.*, 2001). Formation of the Martian crustal dichotomy (Watters *et al.*, 2007) and Tharsis occurred very early in the planet's history (e.g., Anderson *et al.*, 2001; Dohm *et al.*, 2001b, 2007a; Phillips *et al.*, 2001; Frey *et al.*, 2002; Nimmo and Tanaka, 2005; Frey, 2006), yet the structures from those Noachian times, as much as 4 Ga ago (Frey, 2006), are

well preserved on Mars, in part due to the thin atmosphere that promotes slow rates of erosion and deposition relative to the Earth (e.g., Schultz, 1999) and in part due to the general lack of subsequent deformational events. On the other hand, other works indicate that the dichotomy could have evolved for a more extended period, possibly related to plate tectonics (Fairén and Dohm, 2004; Baker *et al.*, 2007). As a result, Martian structures have been used extensively to construct and test models for the internal evolution of the planet (e.g., Wise *et al.*, 1979; Banerdt *et al.*, 1982, 1992; Tanaka *et al.*, 1991; Márquez *et al.*, 2004; Dimitrova *et al.*, 2006; Baker *et al.*, 2007; Golombek and Phillips, Chapter 5).

The most common types of structures on Mars – grabens, thrust faults, and wrinkle ridges – demonstrate the predominance of extensional and contractional deformation, respectively, of the planet's crust or lithosphere (Plate 24; see Tanaka *et al.*, 1991; Scott and Dohm, 1997; Dohm and Tanaka, 1999; Schultz, 2000a; Dohm *et al.*, 2001a,b; Knapmeyer *et al.*, 2006; Schultz *et al.*, 2007; Golombek and Phillips, Chapter 5). However, Mars also displays clear evidence of strike-slip faulting (Forsythe and Zimbelman, 1988; Schultz, 1989; Okubo and Schultz, 2006). Recent work using high-resolution MOLA topography has identified the surface expression of igneous dikes in Tharsis (Schultz *et al.*, 2004; Goudy and Schultz, 2005).

The formation of Tharsis produced a vast system of grabens and wrinkle ridges that span the entire western hemisphere (Anderson *et al.*, 2001; Montesi and Zuber, 2003a,b). In contrast, grabens primarily accompanied the formation of Elysium (Carr, 1974; Wise *et al.*, 1979; Plescia and Saunders, 1982; Tanaka and Davis, 1988; Tanaka *et al.*, 1991; Banerdt *et al.*, 1992). Many of the grabens and wrinkle ridges associated with these regions, along with normal faults, dikes, and rifts, display a geometric relationship between the center of the magmatic-tectonic regions and the structures (Schultz, 1985; Watters and Maxwell, 1986; Tanaka *et al.*, 1991; Watters, 1993; Anderson *et al.*, 2001; Phillips *et al.*, 2001; Schultz *et al.*, 2006). Most of the structures identified within the Tharsis and Elysium regions are grabens (e.g., Tanaka and Davis, 1988; Tanaka *et al.*, 1991; Davis *et al.*, 1995; Anderson *et al.*, 2001). In places, grabens are associated with pit crater chains (e.g., Schultz, 1991; Okubo and Schultz, 2003; Wyrick *et al.*, 2004; Ferrill *et al.*, 2004; Goudy and Schultz, 2005). Rift-sized grabens, primarily located in the Tharsis region, have widths that generally range between 10 and 100 km and depths up to a few kilometers (e.g., Plate 25). Such large grabens are characterized by multiply faulted borders and floors (e.g., Plescia and Saunders, 1982; Dohm and Tanaka, 1999; Wilkins *et al.*, 2002; Wilkins and Schultz, 2003) and resemble complex terrestrial rift systems (Schultz, 1991, 1995; Banerdt *et al.*, 1992; Hauber and Kronberg, 2005). Other extensional structures include the Valles Marineris troughs (e.g., Blasius *et al.*, 1977; Lucchitta *et al.*, 1992; Mège and Masson, 1996; Schultz, 1991, 1995, 1998, 2000b; Wilkins and Schultz, 2003), structurally

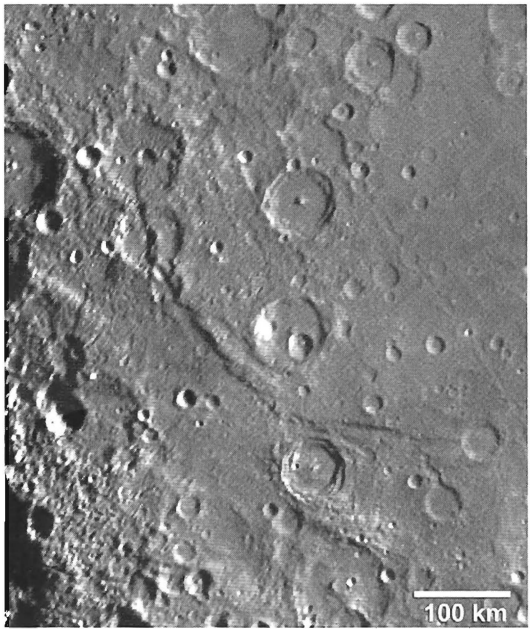

Figure 8.6. Mariner 10 mosaic of Hero Rupes. Hero Rupes (58°S, 173°W) is one of the many large-scale lobate scarp thrust faults in the portion of the southern hemisphere imaged by Mariner 10.

controlled sapping channels (e.g., Davis *et al.*, 1995), and troughs of polygonal patterned ground (e.g., Pechmann, 1980; McGill, 1986; McGill and Hills, 1992; Buczkowski and McGill, 2002). Wrinkle ridges occur across the Martian surface (e.g., Chicarro *et al.*, 1985; Watters and Maxwell, 1986; Watters, 1988; Schultz, 2000a; Goudy *et al.*, 2005) and formed in association with impact basins, as on the Moon, and volcanotectonic provinces such as Tharsis, Thaumasia, and Elysium.

3.3 Mercury

In 1974 and 1975, the Mariner 10 spacecraft made three flybys of Mercury, returning over 2700 images of the eastern hemisphere, covering about 45% of the planet's surface (Strom, 1984). The resolution of images varied greatly from 100 to 4000 m/pixel. The three encounters of Mariner 10 occurred when the same hemisphere was illuminated. With the subsolar point located at about 0°N, 100°W, much of the imaged hemisphere had poor illumination geometry (near-nadir solar incidence) for the identification of tectonic landforms and morphologic features. In early 2008, MESSENGER became only the second spacecraft to visit Mercury. In the first of three flybys that will lead to Mercury orbit in 2011, MESSENGER imaged about 21% of the hemisphere unseen by Mariner 10 (Solomon *et al.*, 2008).

Landforms indicative of crustal shortening and extension are clearly evident on Mercury (Strom *et al.*, 1975; Melosh and McKinnon, 1988; Watters *et al.*, 2004;

Watters and Nimmo, Chapter 2). Lobate scarps, interpreted to be thrust faults, are the most widely distributed tectonic feature (Figure 8.6; Strom *et al.*, 1975; Melosh and McKinnon, 1988; Watters *et al.*, 1998, 2004; Solomon *et al.*, 2008). These faults occur throughout the imaged regions and deform the oldest intercrater plains and the youngest smooth plains (Watters and Nimmo, Chapter 2). A rare, related tectonic feature on Mercury are high-relief ridges. The maximum relief of high-relief ridges can exceed 1 km, and they appear to be spatially and temporally associated with lobate scarps. Deforming the same units as lobate scarps, in some cases, high-relief ridges transition into lobate scarps (Watters *et al.*, 2004; Watters and Nimmo, Chapter 2).

Wrinkle ridges are another common tectonic landform on Mercury, although they are not as broadly distributed as lobate scarps. Wrinkle ridges occur predominantly in smooth plains in the interior of the Caloris basin and in the smooth plains exterior to the basin (Strom *et al.*, 1975; Melosh and McKinnon, 1988; Watters *et al.*, 2005; Watters and Nimmo, Chapter 2).

Surprisingly, Mercury displays few extensional landforms in the imaged regions. Evidence of widespread extension is only found in the interior plains materials of the Caloris basin (Strom *et al.*, 1975; Melosh and McKinnon, 1988; Watters *et al.*, 2005; Murchie *et al.*, 2008; Watters and Nimmo, Chapter 2). Basin-radial and basin-concentric grabens form a remarkably complex pattern of extension (Murchie *et al.*, 2008; Watters and Nimmo, Chapter 2). This network of grabens crosscuts the wrinkle ridges in the Caloris basin (Strom *et al.*, 1975; Melosh and McKinnon, 1988; Watters *et al.*, 2005; Murchie *et al.*, 2008; Watters and Nimmo, Chapter 2).

Post Mariner 10 models for the origin of the tectonic stresses on Mercury involve global contraction due to secular cooling of the interior, tidal despinning, a combination of global contraction and tidal despinning, or a combination of global thermal contraction and the formation of the Caloris basin (Strom *et al.*, 1975; Cordell and Strom, 1977; Melosh and Dzurisin, 1978a,b; Pechmann and Melosh, 1979; Melosh and McKinnon, 1988; Thomas *et al.*, 1988; Thomas, 1997). These models predict distinctive patterns of tectonic features. Global contraction from slow thermal cooling results in global, horizontally isotropic compression (Solomon, 1976, 1977, 1978, 1979; Schubert *et al.*, 1988; Phillips and Solomon, 1997; Hauck *et al.*, 2004), predicting uniformly distributed, randomly oriented thrust faults. Tidal despinning predicts N–S oriented thrust faults in the equatorial zone and E–W normal faulting in the polar regions (Melosh and Dzurisin, 1978a,b; Melosh and McKinnon, 1988). Stresses related to the formation of the Caloris basin might result in Caloris-radial thrust faults (Thomas *et al.*, 1988; Thomas, 1997). Recent modeling suggests that mantle convection may be another important source of stress on Mercury (King, 2008). The spatial and temporal distribution of tectonic features is thus critical to constraining existing models for the origin of the stresses

and future models that may emerge when the MESSENGER mission completes a global survey of Mercury (Solomon *et al.*, 2001, 2007).

Early efforts to map Mercury's tectonic features were based largely on the analysis of individual Mariner 10 image frames and hand-lain mosaics (see Strom *et al.*, 1975; Strom, 1984). Tectonic features were also mapped as part of the 1:5 000 000 geologic map series of Mercury (e.g., Schaber and McCauley, 1980) based on a series of shaded relief maps at the same scale (Davies and Batson, 1975; Davies *et al.*, 1978). Recent efforts to map tectonic features imaged by Mariner 10 involve digitization directly from image mosaics with improved radiometry and geometric rectification (Robinson *et al.*, 1999; Watters and Nimmo, Chapter 2). The less than ideal lighting geometry over much of the hemisphere imaged by Mariner 10 (incidence angles $<45°$) introduces an observational bias that must be considered (Watters *et al.*, 2004). In some areas imaged by Mariner 10, the limitations of the poor illumination geometry can be overcome by the availability of stereo coverage. Topography generated from stereo pairs helps to reveal tectonic landforms not easily detected in Mariner 10 images (see Watters *et al.*, 2001, 2002). The importance of illumination geometry in identifying tectonic landforms has been demonstrated by MESSENGER where previously undetected lobate scarps have been found near the Mariner 10 subsolar point (Solomon *et al.*, 2008; Watters and Nimmo, Chapter 2).

A tectonic map of lobate scarps imaged by Mariner 10 shows that they are unevenly distributed with preferred orientations, east-trending compressional tectonic features in the polar regions, and no dominant Caloris-radial pattern of lobate scarps (see Watters and Nimmo, Chapter 2). This suggests that some models for the global tectonic stresses do not fully account for the spatial distribution of the known tectonic landforms (see also Watters and Nimmo, Chapter 2, for a review of Mercury tectonics).

3.4 Venus

Venusian tectonic structures range from broad lowland basins to narrow linear features (e.g., Solomon *et al.*, 1992). The major global datasets for mapping structures include NASA Magellan mission high-resolution gravity, altimetry, and synthetic aperture radar (SAR) data. Given the long wavelength of gravity (resolves features >400 km) and altimetry ($\sim$20 km footprint) data, SAR imagery ($\sim$100 m/pixel) proves most useful for structural element identification. The morphology of Venusian structures is more readily visualized using inverted SAR images (Figures 8.7–8.10).

Regional geomorphic groups include lowland basins, linear deformation belts ($\sim$20–150 km wide, 1000's of km long) in either parallel or polygonal distribution,

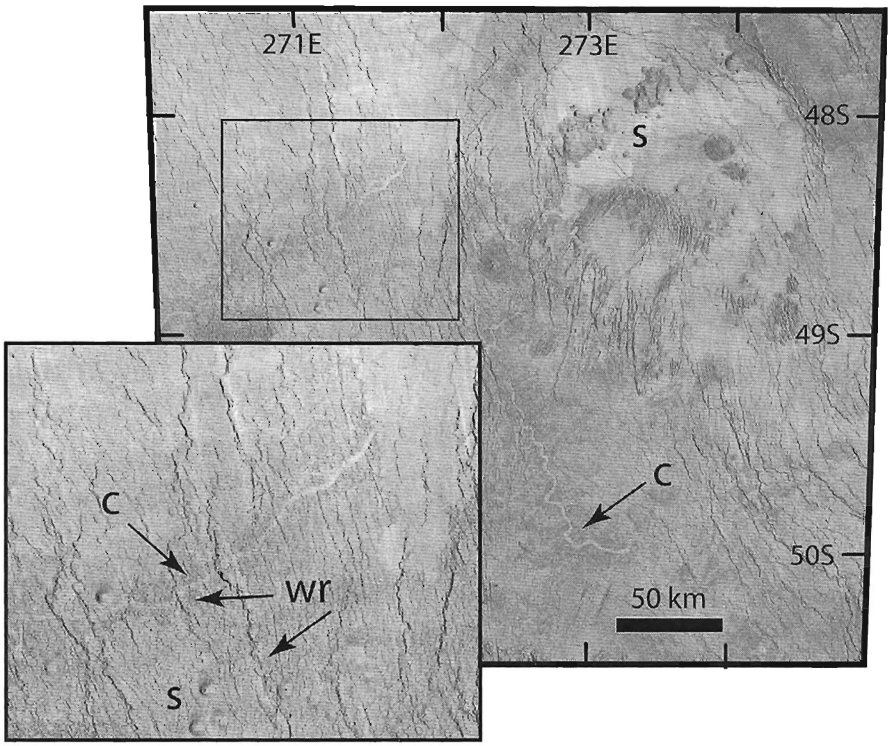

Figure 8.7. Shields and associated lava flows (e.g., Guest *et al.*, 1992; Addington, 2001; Hansen, 2005) in part of Helen Planitia variably bury kipukas of relatively high-standing deformed terrain in the NE corner. Variably spaced NNW-trending wrinkle ridges transect the area. Wrinkle ridges are less developed where shields and kipukas outcrop, either because shield lavas partly buried the wrinkle ridges or because mechanical differences between the host rocks favored wrinkle-ridge formation in the adjacent, lowland plains over the shield and kipuka terrains. Changes in wrinkle-ridge spacing could also reflect local differences in rheology or surface history; for example: (1) the area could have been deformed by closely spaced wrinkle ridges, then locally covered by a thin surface layer (NE corner of inset), followed by formation of widely spaced wrinkle ridges across the region; (2) closely and widely spaced wrinkle ridges could have formed synchronously, followed by local emplacement of a surface layer that covered closely spaced wrinkle ridges in the NE corner of the inset; and (3) surface flows of various layer thickness and coverage could have extended variably across the inset region; later formed wrinkle ridges (short and longer wavelength) could have formed generally synchronously, with wavelength reflecting the variable thickness (and/or strength) of individual surface units. Each of these histories can be accommodated within the context of the image data, and each should be considered as equally viable possibilities. Two channel segments (c) could represent a single channel (joining beneath the shield terrain) or two separate channels. Careful examination (see inset) indicates that a range of temporal relations among channel, shield (s) and wrinkle ridge (wr) formation are preserved. (Inverted Magellan SAR image mosaic; 75 m/pixel.)

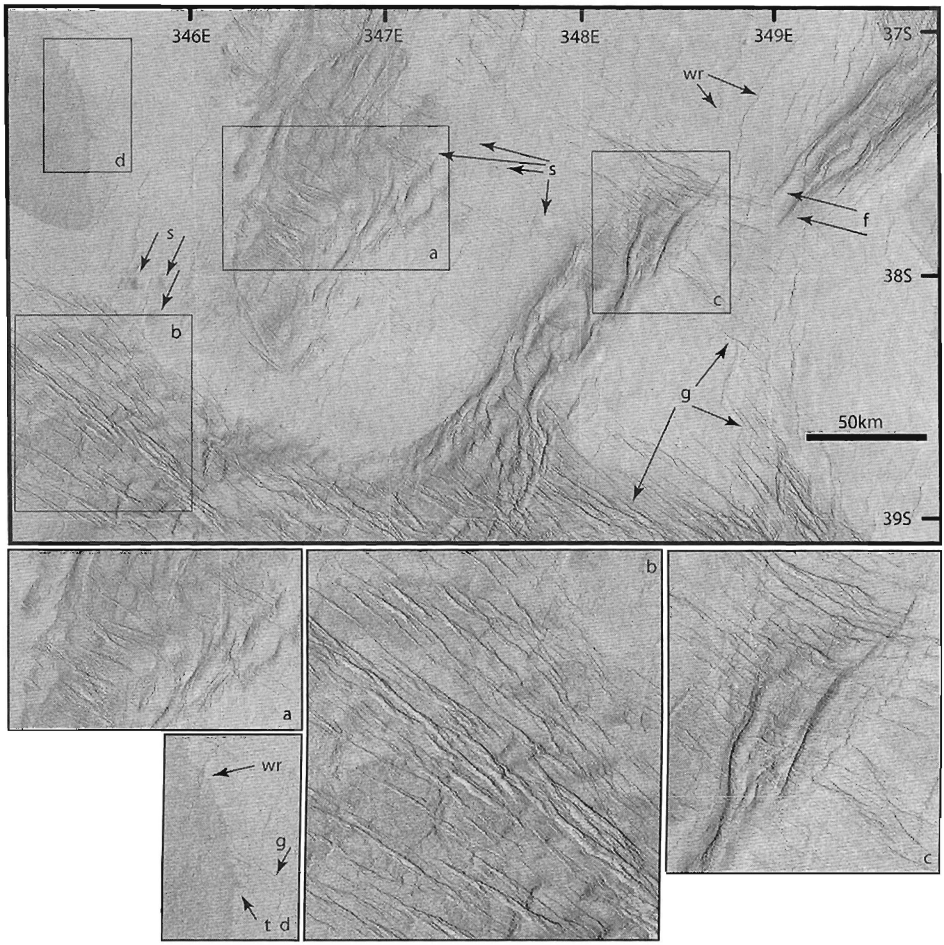

Figure 8.8. Lavinia Planitia hosts deformation belts that display NE-trending folds and NW-trending grabens. In the regions between deformation belts, wrinkle ridges parallel fold trends and grabens (or extension fractures) parallel graben trends in deformation belts. Note the gradational change in radar backscatter across fold crests and wrinkle ridges. Local radar backscatter boundaries show spatial relations with folds (a) and grabens (d) that indicate low-viscosity material embayed preexisting structural topography; elsewhere (b) radar backscatter boundaries show no spatial correlation with structural elements, indicating that backscatter boundaries pre-date fold and graben formation. In some cases, the change in radar backscatter is likely a function of structure topography and not related to different surface layers (e.g., c). Thus across this region, evidence for different surface histories can be gleaned. Although relatively clear embayment relations in the western part of inset a indicate that a low-viscosity surface layer was emplaced following both fold and graben formation, there is no evidence for material embayment following tectonism at location c. Here the distribution of folds and grabens appears to be a function of original strain partitioning, with strain intensity decreasing away from the deformation belt. At location d the embayed grabens presumably formed prior to the western surface unit, which predated local wrinkle-ridge formation. (Inverted Magellan SAR image mosaic; 75 m/pixel.)

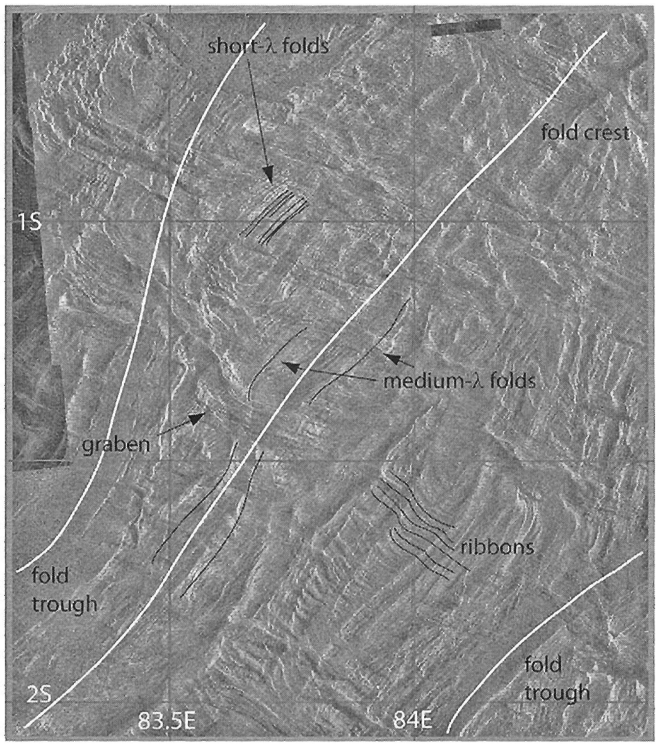

Figure 8.9. Part of Ovda Regio showing typical tessera terrain structures, including grabens, ribbons, and variable wavelength folds. White lines indicate troughs and crest of long-wavelength folds. See text for discussion. (Inverted Magellan SAR image mosaic; 75 m/pixel.)

large (~1000–2500 km diameter) quasi-circular domes (volcanic rises) and plateaus (crustal plateaus), linear troughs (up to ~400 km wide, 1000's of km long) called chasmata, and ~500 quasi-circular features (60–600 km diameter; Stofan *et al.*, 1992, 2001) called coronae. Each of the regional geomorphic groups preserves a combination of individual structural elements. Smaller scale geomorphic features include ~970 impact craters (~1–280 km diameter; Phillips *et al.*, 1992; Schaber *et al.*, 1992; Herrick *et al.*, 1997), medium to small volcanoes, relatively rare pancake domes, and tens to hundreds of thousands of 1–5-km diameter shields (Guest *et al.*, 1992; Crumpler *et al.*, 1997).

SAR's sensitivity to topography makes it an excellent tool for identifying primary landforms (i.e., intrinsic features of geologic map units) such as shield volcanoes, channels, levees, lava flow fronts, pit chains, and impact craters, as well as tectonic structures such as fault scarps, fold ridges, wrinkle ridges, and grabens (Figures 8.7–8.10; for additional discussion, see Ford *et al.*, 1993). The relief of most of the smaller deformational structures is poorly expressed in SAR images, requiring

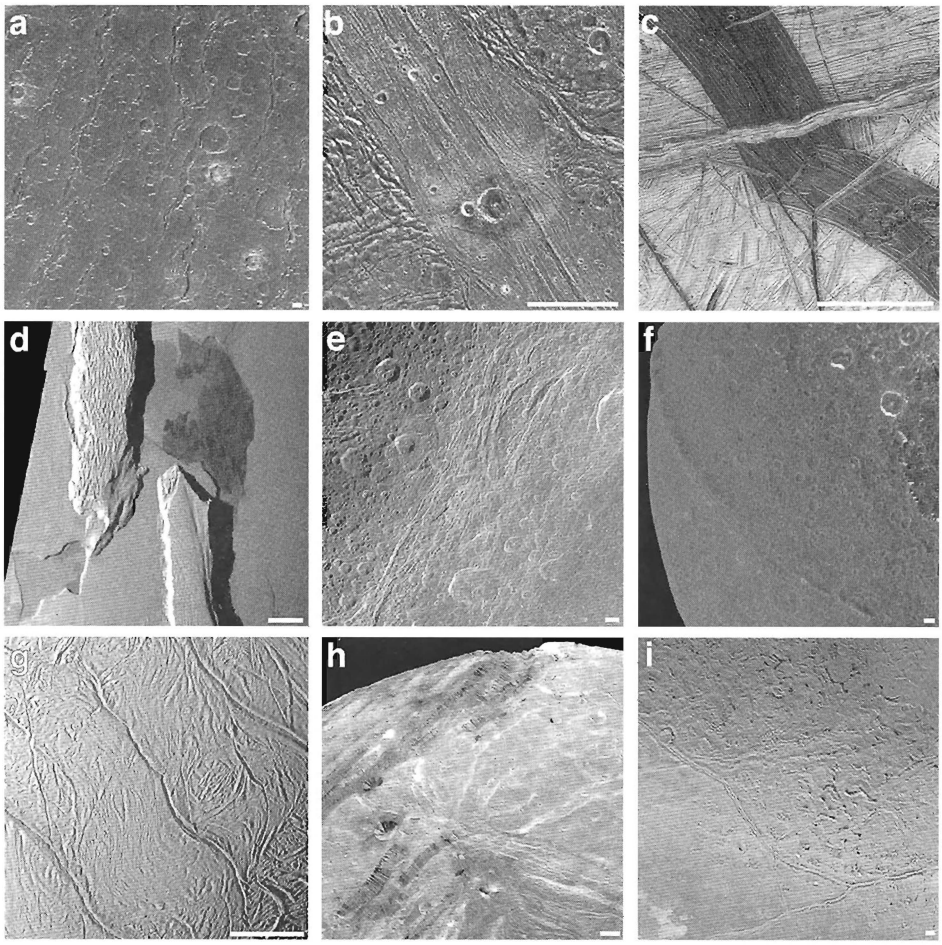

Figure 8.10. A montage of structures on several of the large and mid-sized outer planet satellites. Scale bars are each 20 km long. (a) Callisto: furrows surround the multiringed structure Valhalla. (b) Ganymede: grooved terrain of Byblus Sulcus is straddled by parallel and sub-orthogonal furrows in dark terrain. (c) Europa: the dark band Yelland Linea cuts older ridged plains and was subsequently overprinted by a prominent double ridge. (d) Io: mountains ~3.5 km tall adjacent to the dark-floored caldera Hi'iaka Patera. (e) Dione: fault scarps reveal brighter subsurface ice to create the satellite's wispy terrain. (f) Iapetus: a 20-km high ridge runs along the satellite's equator. (g) Enceladus: prominent fractures that cut across the satellite's south polar region are the sites of active venting. (h) Miranda: Inverness Corona (foreground) and Arden Corona (limb) are the sites of normal faulting, likely triggered by interior upwelling. (i) Triton: graben-like troughs in a region transitional from smooth terrain, which shows evidence for cryovolcanism, to the pitted "cantaloupe terrain," which may have formed by diapirism.

that their morphologic analysis relies heavily on their plan form. However, there is a rich record of their forms, orientations, distributions, and interactions with various features that assist with determination of their relative ages. In some cases, features display evidence of multiple episodes of activity. Figures 8.7 and 8.8 demonstrate this varied record and how multiple interpretations are commonly possible regarding relative ages of structures, and what mechanisms and factors control structural characteristics such as form, orientation, and spacing. Broad generalizations about their origin and age therefore cannot be made with certainty.

Tessera or tessera terrain (Figure 8.9) was originally called parquet terrain (in reference to its reticulate structural patterns). Tessera terrain, preserved in highland crustal plateaus and lowland regions and widely interpreted as collapsed plateaus (e.g., Ivanov and Head, 1996; Phillips and Hansen, 1994), consists of folds of multiple wavelengths, grabens, and variably flooded regions (Hansen and Willis 1996, 1998; Ghent and Hansen, 1999; Hansen, 2006). Discernible fold sets of common orientation have characteristic wavelengths that range from 0.3 km, the limit of effective SAR resolution, to ~100 km. Extensional structures, represented by long-aspect-ratio ribbon (steep-sided, graben-like) structures (Hansen and Willis, 1998) and shorter aspect ratio grabens, generally trend normal to fold crests. Cross-cutting relations, as well as mechanical arguments, illustrate that contractional and extensional structures formed broadly synchronously with the evolution of progressively longer wavelength structures with time (Hansen and Willis, 1998; Ghent and Hansen, 1999; Hansen *et al.*, 2000; Banks and Hansen, 2000; Hansen, 2006). Low-viscosity material, presumably lava, fills local structural lows; lava fill occurs both within troughs of long-wavelength folds and within structural lows along the crests and limbs of long-wavelength folds, indicating that flooding occurred throughout the development of the structural fabric (Hansen, 2006). Fold wavelength records progressively smaller amounts of shortening with a 0.3-km fold wavelength recording minimum shortening of ~30–40%, whereas 50- to 100-km wide folds record <1% layer shortening, indicating progressive fold formation of short- to long-wavelength folds with increasing layer thickness above a low-viscosity material, presumably lava (Hansen, 2006). For an alternative view of tessera terrain evolution, see Gilmore *et al.* (1998).

Ribbons (Figure 8.9) comprise alternating parallel ridges and troughs. Ribbons occur as suites of (listric?) normal faults with ramped trough terminations, and tensile fracture ribbons that show V-shaped terminations and matching opposing trough walls (Hansen and Willis, 1998).

Considerable progress has been made in mapping structures on Venus. Deformed terrains characterized by tessera, fold belts, fracture zones, and coronae have been delineated globally (e.g., Stofan *et al.*, 1992; Price and Suppe, 1995; Ivanov and Head, 1996). Although globally averaged crater statistics indicate that the mean

crater densities of these terrains may vary, they provide little constraint for dating structures. Such inferences rely on crater statistics of the surfaces that host particular structures rather than the structures themselves; untestable assumptions include (1) the host surface was formed relatively quickly, and (2) the structures formed all at once, and immediately following the host surface. Therefore, the uncertainties in the crater statistics are large, permitting a wide range of plausible histories (Tanaka *et al.*, 1997; Campbell, 1999). The general paucity of reliable, spatially broad relative-age indicators along with complex geologic activity across the Venusian surface prevent construction of detailed structural histories at regional scales (e.g., Young and Hansen, 2003), as has been done for other planets and satellites such as the Moon and Mars. Thus resolving whether or not Venus underwent global catastrophic stratigraphic and structural events (e.g., Basilevsky and Head, 1998) or sporadic, regional activity at various times (Guest and Stofan, 1999), or a general evolution of spatially and temporally definable processes (e.g., Phillips and Hansen, 1998) will require detailed global mapping.

3.5 Outer planet satellites

The six large satellites (radius $\geq$1300 km) and 12 mid-sized satellites (radius $\geq$ 200 km) of the outer planets display a wide range of structures in diverse settings across four different planetary systems (Figure 8.10). Reconnaissance of the satellites was achieved by the Voyager 1 and 2 spacecraft, which surveyed all four planetary systems over the decade of 1979 to 1989 (with imaging resolutions lower than several hundred meters per pixel), followed by detailed and significantly higher resolution imaging (areas as high as several meters per pixel) by the Galileo spacecraft in orbit about Jupiter from 1995 to 2003, and the Cassini spacecraft, which began orbiting Saturn in 2004. A thorough review of the tectonics of outer planet satellites is provided by Collins *et al.* (Chapter 7).

Identification of structures on these satellites is complicated by materials, processes, and landforms that may be unfamiliar to the terrestrial geologist. With the notable exceptions of rocky Io and volatile-rich Triton, their surfaces are composed primarily of H_2O ice and various non-ice contaminants, whereas some contain other volatile components, such as CO_2 and SO_2. Unlike the terrestrial planets, global-scale tectonic processes are commonly linked to changes in satellite shape induced by tidal interactions with their parent planet, including despinning, orbital recession/procession, and reorientation relative to the tidal axes (nonsynchronous rotation or true polar wander). Volume change resulting from internal thermal evolution is also quite plausible, including thermal expansion or contraction, ice-phase transitions, or compositional differentiation. The variety of tectonic landforms is discussed below, organized by planetary system.

The only formal maps of the outer planet satellites generated to date are Voyager-based maps of the Galilean satellites of Jupiter; revisions to several of these maps are in progress, based on Galileo data. Structural mapping follows the definition and procedures outlined for the terrestrial planets, although some heavily tectonized material units (e.g., Ganymede's grooved terrain) necessarily are defined by their structural fabric (Wilhelms, 1990). The complexity of structural relationships combined with limitations of the available data make determination of relative ages difficult. Moreover, absolute age is poorly constrained, because the outer solar system impactor population has likely been different from that of the inner solar system, and it is difficult to extrapolate the current-day fluxes of observationally detected impactors back through time (Zahnle *et al.*, 2003; Schenk *et al.*, 2004).

Callisto. Of Jupiter's four Galilean satellites, Callisto's structural geology, dominated by exogenic processes, is by far the simplest (Moore *et al.*, 2004a). Callisto's impact craters show a variety of forms, from small bowl-shaped basins, through larger complex craters with central peaks, analogous to those on the Moon or Mercury. Unlike craters on the terrestrial planets, craters >35 km show central pits and those >60 km display central domes on both Callisto and Ganymede (Schenk *et al.*, 2004), perhaps due to the effect of subsurface ductile ice during the impact process (Schenk, 1993). Several large multiringed structures on Callisto (typified by Valhalla and Asgard) consist of sets of concentric ridges and/or scarps that are hundreds of kilometers in extent (Figure 8.10a) (Schenk and McKinnon, 1987). These probably surround the sites of large impact events that penetrated to a low-viscosity zone, plausibly a subsurface ocean >100 km beneath the surface, inducing surface extension that created concentric normal faults as the transient crater collapsed (McKinnon and Melosh, 1980; Schenk *et al.*, 2004). An induced magnetic field signature implies a briny ocean within Callisto today (Kivelson *et al.*, 1999), but the lack of endogenic activity means that this ocean is manifest at the surface probably only in the satellite's ancient impact-induced tectonics.

Ganymede. The surface of Ganymede (Pappalardo *et al.*, 2004) consists of about 1/3 dark terrain, which is heavily cratered and ancient, and 2/3 bright grooved terrain, which is less cratered and more recent (Figure 8.10b). Dark terrain contains arcuate systems of tectonic furrows, likely remnants of multiringed structures like those on Callisto (Schenk and McKinnon, 1987; Murchie and Head, 1988), and perhaps similarly an indication of a subsurface ocean (Schenk *et al.*, 2004); of less certain origin are semi-radial furrows also spatially associated with multiring structures. Ganymede's bright grooved terrain crosscuts the dark terrain in elongated swaths (sulci) that are pervasively tectonized in rift-like fashion (Shoemaker *et al.*, 1982; Pappalardo *et al.*, 2004). Two topographic "wavelengths" of structures occur within grooved terrain: (1) the broader (~8 km) scale is inferred to be related to extensional necking of the icy lithosphere above a ductile ice substrate

(Dombard and McKinnon, 2001), and (2) the finer ($\leq$1 km) scale is inferred to have formed by tilt-block style normal faulting of stretched ice (Pappalardo *et al.*, 2004). Geometrical arguments and deformed impact craters indicate that extensional strain reaching tens of percent may be common in grooved terrain (Collins *et al.*, 1998; Pappalardo and Collins, 2005). A component of this strain includes strike-slip displacement (Pappalardo *et al.*, 2004).

Grooved terrain may be brightened and smoothed by a combination of faulting, which exposes bright ice from beneath a dark surface veneer of impactor debris, and icy volcanism (cryovolcanism), which resurfaces older dark terrain (Shoemaker *et al.*, 1982; Schenk *et al.*, 2001a; Pappalardo *et al.*, 2004). Scalloped depressions (paterae) are associated with some smooth lanes, and these may be caldera-like volcanotectonic features associated with cryovolcanism (Schenk *et al.*, 2001a). The extensional strain recorded within Ganymede's grooved terrain has been attributed to early differentiation and associated ice-phase changes and global expansion (Squyres, 1980), and attempts have been made to constrain the global degree of expansion that is consistent with geological observations (McKinnon, 1982; Golombek, 1982; Collins, 2006). It remains to be demonstrated how the inferred high degree of local extensional strain can be explained, given that no definitive examples of contractional structures have been identified. Although the age of Ganymede's grooved terrain is poorly constrained, the existence of intrinsic and induced magnetic fields at Ganymede indicate an active dynamo and a contemporary internal ocean (Kivelson *et al.*, 2002). It remains to be demonstrated whether grooved terrain might be an indirect manifestation of an internal ocean, such as related to convection in tidally heated ice above a global subsurface ocean, or of nonsynchronous rotation of a floating ice shell.

Europa. Europa's few large impact structures indicate that the satellite's average surface age is ~60 Myr (Zahnle *et al.*, 2003; Schenk *et al.*, 2004), implying recent tectonic activity and associated resurfacing events. Analogous to those on Callisto and Ganymede, Europa's two known multiringed structures (Tyre and Pwyll) suggest transient crater penetration to a low-viscosity layer, plausibly a water ocean, ~20 km below the icy surface (Schenk *et al.*, 2004). This ice shell thickness is consistent with models of basal tidal heating of a floating ice shell (Ojakangas and Stevenson, 1989; Moore, 2006). Europa's geology is complex and includes severely tectonized ridged plains that resemble a ball of string, with crosscutting troughs, double ridges, and bands (Figure 8.10c) (Greeley *et al.*, 2004). Linear to curvilinear or cycloidal troughs, many displaying raised flanks, are interpreted as near-vertical tensile cracks or shear fractures in Europa's ice shell (Greenberg *et al.*, 1998; Greeley *et al.*, 2004). Ubiquitous ridges are most commonly expressed as double ridges (a ridge pair with a medial trough), whereas some display a complex set of constituent subparallel ridges; modest strike-slip offset along these structures is common. Models of ridge formation include tidal squeezing,

compression, dike intrusion, and localized shear heating (see Collins *et al.*, Chapter 7, for a review). Many ridges show diffuse dark flanks, called triple bands. Bands are linear to curvilinear features up to ~25 km wide, consisting of smooth, lineated, and/or hummocky interiors (Prockter *et al.*, 2002). In many cases, the surrounding terrain can be reconstructed, indicating that bands are sites where the brittle lithosphere was pulled apart and replaced by more mobile material from below. This resurfacing included cracking and/or faulting to form subparallel structures. Likely stress mechanisms for creating Europa's tectonic structures include: (1) diurnal stressing induced by radial and librational tides as Europa rapidly orbits Jupiter, (2) slow nonsynchronous rotation of Europa's ice shell relative to the satellite's tidal axes, and (3) true polar wander inducing change in the shape of the ice shell (Greeley *et al.*, 2004; Collins *et al.*, Chapter 7). The cycloidal shapes of many structures is convincing evidence of the action of diurnal stresses, where the effective speed of a propagating fracture is a close match to the diurnally rotating direction of tensile stress, with the fracture tracing an arc each Europa day (Hoppa *et al.*, 1999a). Moreover, rotating diurnal stresses can produce a preferred sense of strike-slip offset along faults in each hemisphere of Europa (Hoppa *et al.*, 1999b). Diurnal stresses are expected to be significant only if Europa's ice shell is decoupled from the rocky mantle by an ocean (Moore and Schubert, 2000). Therefore, cycloidal features are strong evidence for an ocean when the structures formed, and given the young age of the surface, this must be recently.

Europa's surface is marked by domes (indicative of tectonic uplift of the icy lithosphere) and pits (indicative of withdrawal of surface material and associated lithospheric downwarp). Scattered across the surface, reddish material has extruded to form spots and chaotic terrain, commonly associated with ridged plains deformation (Greeley *et al.*, 2004). In the largest and most dramatic examples (e.g., Conamara Chaos), older ridged plains are tectonically disrupted and blocks have rotated and translated in a hummocky matrix, and much of the original plains has been destroyed. Spots and chaos are attributed to whole-scale melting of Europa's ice shell (Greenberg *et al.*, 1999), or partial melting triggered by diapiric upwellings (Pappalardo *et al.*, 1999); however, the geophysical details of these models have yet to be satisfactorily understood (Nimmo and Giese, 2005). Crosscutting relationships among Europa's tectonic features and chaotic terrains indicate that structural deformation has become more narrowly focused through Europa's preserved history, and that chaotic terrain is overall more recent in the stratigraphy (Figueredo and Greeley, 2004), unless older chaos occurred but has been modified over time (Riley *et al.*, 2000). Recent chaos is consistent with recent ice shell thickening (Pappalardo *et al.*, 1999), perhaps related to secular changes in heat flux due to cyclical variations in orbital eccentricity (Hussmann and Spohn, 2004).

Io. Io is the most volcanically active body in the solar system, with a measured heat flux of ~2 Wm^2, resulting from tidal heating of this rocky satellite (McEwen

et al., 2004). Its landscape is dominated by volcanic calderas (paterae), edifices, and flows, but ~3% of Io's surface consists of mountains that are likely tectonic in origin (Figure 8.10d) (McEwen *et al.*, 2004). Mountains are typically tens of kilometers across, average ~6 km tall, and reach heights of ~17 km. Many mountains are surrounded by debris aprons, evidence of mass wasting of loosely consolidated surface materials. Mountains potentially formed by large-scale up-thrusting of lithospheric blocks in response to global-scale compression, due to the high rate of volcanism and associated vertical loading and cycling (Schenk and Bulmer, 1998). Locally concentrated stress may have triggered mountain formation, such as through mantle diapirism (Turtle *et al.*, 2001; Jaeger *et al.*, 2003). Mountains are most abundant in two antipodal zones on the satellite, and are globally anticorrelated with volcanic centers (Schenk *et al.*, 2001b). Nonetheless, individual mountains and paterae are commonly associated, and some mountains show evidence of rifting, perhaps related to uplift (Jaeger *et al.*, 2003). Kilometer-scale ridges and troughs on the flanks of some mountains might be the expression of folds in a deformable surficial layer, perhaps driven by gravity sliding (Moore *et al.*, 2001). Similar small-scale structures on Io's plains may be contractional structures formed by diurnal tidal stress (Bart *et al.*, 2004).

Satellites of Saturn. As of this writing, the Cassini mission is changing our understanding of the tectonic histories of the Saturnian satellites, but few publications of the results yet exist. Smog-shrouded Titan is being revealed by radar imaging, and by imaging through near-infrared atmospheric windows using both Cassini's camera and infrared instrument (Elachi *et al.*, 2005; Porco *et al.*, 2005a; Sotin *et al.*, 2005). Several large impact craters occur on Titan, and lineaments and linear boundaries could be tectonic. Tectonic features occur on all of Saturn's middle-sized icy satellites. Voyager images revealed bright wispy terrains on both Dione and Rhea, which Cassini imaging has resolved as extensional fault scarps that expose relatively clean subsurface icy material (Figure 8.10e) (Johnson, 2005). Dione and Tethys exhibit ridges that may be contractional in origin (Moore and Ahern, 1983; Moore, 1984). Cassini imaging resolves the detailed internal fault structure of Ithaca Chasma on Tethys, a global-scale rift zone which roughly follows a great circle normal to the center of the impact basin Odysseus and thus may be related to the basin's formation or relaxation (Moore *et al.*, 2004b). Iapetus displays a 20-km high ridge that delineates the satellite's equator (Figure 8.10f), possibly indicating tidal despinning and associated equatorial radius decrease (Porco *et al.*, 2005b). Existing models of the thermal and corresponding tectonic evolution of the Saturnian satellites (Schubert *et al.*, 1986; Hillier and Squyres, 1991) will certainly be modified and improved upon, aiding interpretation of Cassini images.

Enceladus exhibits spectacular active vapor plumes escaping the satellite from prominent, warm tectonic structures in its extremely youthful and tectonically

deformed south polar region (Figure 8.10g) (Porco *et al.*, 2006; Spencer *et al.*, 2006). Overall, it seems that intense tectonism (rather than cryovolcanism) may have resurfaced the youthful parts of Enceladus (Johnson, 2005). Tectonic interpretation of the south polar terrain suggests shortening of the satellite's spin axis (Porco *et al.*, 2006), consistent with true polar wander of Enceladus to move a low-density internal mass anomaly to the spin axis (Nimmo and Pappalardo, 2006). Prominent tectonic structures in the south polar terrain, nicknamed "tiger stripes," may have formed as tension fractures and are believed to undergo shearing and open–close motions through the Enceladus tidal cycle, probably playing an important role in the production and release of the satellite's vapor plumes (Hurford *et al.*, 2007; Nimmo *et al.*, 2007; Spitale and Porco, 2007; Smith-Konter and Pappalardo, 2007). The mechanisms for tectonic deformation of Enceladus, and the possible role of an internal ocean or sea (Collins and Goodman, 2007; Nimmo *et al.*, 2007), will continue to be important topics of investigation.

Satellites of Uranus. The Voyager 2 spacecraft passed closest to the innermost of the five major Uranian satellites, so imaging resolution is best at Miranda, while Titania and Oberon were not imaged sufficiently to resolve tectonic structures. Umbriel appears generally featureless and dark, but careful image processing reveals an ancient tectonic system (Helfenstein *et al.*, 1989). Ariel displays a global-scale structural pattern of tectonic rifts, ridges, and troughs forming an obliquely intersecting pattern across much of the satellite's visible surface (Plescia, 1987). Some rift depressions appear to have been resurfaced by a viscous cryolava (Jankowski and Squyres, 1988). Abundant extensional tectonic structures on many of the Uranian satellites, as on the Saturnian satellites, are attributed to volume changes linked to thermal evolution (Schubert *et al.*, 1986; Hillier and Squyres, 1991).

Despite its small size, Miranda exhibits striking structural geology (Figure 8.10h). Miranda displays three ovoidal regions termed "coronae" that are deformed by subparallel ridges and grooves. An early interpretation of the coronae suggested that they might be folds, which would be consistent with a "sinker" model, in which the satellite was disrupted early in its history by a large impact, with remnants of the proto-satellite's rocky core sinking downward through the reforming satellite and stirring downwelling currents to create the coronae above (Janes and Melosh, 1988). However, subsequent analyses showed that the coronae are likely extensional tectonic structures, including tilted blocks and cryovolcanic extrusions, more consistent with a model in which the coronae formed by tectonic deformation above large-scale upwelling plumes (Greenberg *et al.*, 1991; Schenk, 1991; Pappalardo *et al.*, 1997). Additional tectonic stress may have resulted from reorientation of Miranda in response to corona formation (Plescia, 1988).

Triton. The single large satellite of Neptune, Triton, has a surface rich in exotic ices (CO, CO_2, CH_4, and N_2), in addition to H_2O (Cruikshank *et al.*, 2000). A

variety of structures occur across its surface (Figure 8.10i), including troughs, double ridges, and active geysers, as well as morphological evidence for past cryovolcanism (Croft *et al.*, 1995). Because Triton has a retrograde orbit, it is generally believed that Triton is a captured body that originated as a Kuiper Belt object (Agnor and Hamilton, 2006). Triton's tectonic patterns may be influenced by its orbital procession as it spirals slowly inward toward Neptune, or by other global tectonic stresses (Croft *et al.*, 1995; Collins *et al.*, Chapter 7). Morphological comparison of Triton's ridges to smaller double ridges on Europa has prompted the suggestion that diurnal stressing and shear heating may have contributed to formation of Triton's ridges during the circularization of Triton's orbit following capture (Prockter *et al.*, 2005). Triton displays a unique region known informally as "cantaloupe terrain," where compositionally induced diapirism may have led to crustal overturn to form the pits (cavi) characteristic of this unusual region (Schenk and Jackson, 1993).

Overall, the diverse and sometimes bizarre tectonics of the outer planet satellites is inherently linked to satellite tides and the mechanical–rheological properties of ice (Collins *et al.*, Chapter 7). Our terrestrial experience is critical to their interpretation, yet is challenged by their unfamiliarity.

Acknowledgments

We would like to acknowledge Ron Greeley and Matt Golombek for their review comments that led to improvement of our chapter. Portions of this work performed by RA and RP were carried out at the Jet Propulsion Laboratory, California Institute of Technology, under a contract with the National Aeronautics and Space Administration. This work was also supported by the National Aeronautics and Space Administration under Grants issued through the Office of the Planetary Geology and Geophysics Program.

References

Addington, E. A. (2001). A stratigraphic study of small volcano clusters on Venus. *Icarus*, **149**, 16–36.

Agnor, C. B. and Hamilton, D. P. (2006). Neptune's capture of its moon Triton in a binary–planet gravitational encounter. *Nature*, **441**, 192–194.

Anderson, R. C., Dohm, J. M., Golombek, M. P., Haldemann, A., Franklin, B. J., Tanaka, K., Lias, J. and Peer, B. (2001). Significant centers of tectonic activity through time for the western hemisphere of Mars. *J. Geophys. Res.*, **106**, 20 563–20 585.

Avery, T. E. and Berlin, G. L. (1992). *Fundamentals of Remote Sensing and Airphoto Interpretation*, 5th edn. New York: Macmillan.

Baker, V. R., Maruyama, S., and Dohm, J. M. (2007). Tharsis superplume and the geological evolution of early Mars. In *Superplumes: Beyond Plate Tectonics*, eds. D. A. Yuen, S. Maruyama, S.-I. Karato and B. F. Windley. London: Springer, pp. 507–523.

Baldwin, R. B. (1963). *The Measure of the Moon.* Chicago: University of Chicago Press.
Banerdt, W. B., Phillips, R. J., Sleep, N. H., and Saunders, R. S. (1982). Thick-shell tectonics on one-plate planets: Applications to Mars. *J. Geophys. Res.*, **87**, 9723–9733.
Banerdt, W. B., Golombek, M. P. and Tanaka, K. L. (1992). Stress and tectonics on Mars. In *Mars*, eds. H. H. Kieffer, B. M. Jakosky, C. W. Snyder and M. S. Matthews. Tucson, AZ: University of Arizona Press, pp. 249–297.
Banks, B. K. and Hansen, V. L. (2000). Relative timing of crustal plateau magmatism and tectonism at Tellus Regio, Venus. *J. Geophys. Res.*, **105**, 17 655–17 668.
Bart, G. D., Turtle, E. P., Jaeger, W. L., Keszthelyi, L. P., and Greenberg, R. (2004). Ridges and tidal stress on Io. *Icarus*, **169**, 111–126.
Basilevsky, A. T. and Head, J. W. (1998). The geologic history of Venus: A stratigraphic view. *J. Geophys. Res.*, **103**, 8531–8544.
Bell, J. F., III, Campbell, B. A., and Robinson, M. S. (1999). Planetary geology. In *Remote Sensing for the Earth Sciences: Manual of Remote Sensing*, ed. A. N. Rencz. *3rd edn*, Vol. 3. New York: John Wiley & Sons, pp. 509–563.
Binder, A. B. (1982). Post-Imbrian global lunar tectonism: Evidence for an initially totally molten moon. *Earth Moon Planets*, **26**, 117–133.
Binder, A. B. and Gunga, H. C. (1985). Young thrust-fault scarps in the highlands: Evidence for an initially totally molten Moon. *Icarus*, **63**, 421–441.
Blasius, K. R., Cutts, J. A., Guest, J. E., and Masursky, H. (1977). Geology of the Valles Marineris: First analysis of imaging from the Viking 1 orbiter primary mission. *J. Geophys. Res.*, **82**, 4067–4091.
Buczkowski, D. L. and McGill, G. E. (2002). Topography within circular grabens: Implications for polygon origin, Utopia Planitia, Mars. *Geophys. Res. Lett.*, **29**, doi:10.1029/2001GL014100.
Campbell, B. A. (1999). Surface formation rates and impact crater densities on Venus. *J. Geophys. Res.*, **104**, 21 951–21 955.
Carr, M. H. (1974). Tectonism and volcanism of the Tharsis region of Mars. *J. Geophys. Res.*, **79**, 3943–3949.
Chicarro, A. F., Schultz, P. H., and Masson, P. (1985). Global and regional ridge patterns on Mars. *Icarus*, **63**, 153–174.
Collins, G. C. (2006). Global expansion of Ganymede derived from strain measurements in grooved terrain (abs.). *Lunar Planet. Sci. Conf. XXXVII*, 2077. Houston, TX: Lunar and Planetary Institute (CD-Rom).
Collins, G. C. and Goodman, J. C. (2007). Enceladus' south polar sea. *Icarus*, **189**, 72–82.
Collins, G. C., Head III, J. W., and Pappalardo, R. T. (1998). Role of extensional instability in creating Ganymede grooved terrain: Insights from Galileo high-resolution stereo imaging. *Geophys. Res. Lett.*, **25**, 233–236.
Cook, A. C., Watters, T. R., Robinson, M. S., Spudis, P. D., and Bussey, D. B. J. (2000). Lunar polar topography derived from Clementine stereoimages. *J. Geophys. Res.*, **105**, 12 023–12 034.
Cordell, B. M. and Strom, R. G. (1977). Global tectonics of Mercury and the Moon. *Phys. Earth Planet. Inter.*, **15**, 146–155.
Croft, S. K., Kargel, J. S., Kirk, R. L., Moore, J. M., Schenk, P. M., and Strom, R. G. (1995). Geology of Triton. In *Neptune*, eds. J. T. Bergstralh *et al.* Tucson, AZ: University of Arizona Press, pp. 879–948.
Cruikshank, D. P., Schmitt, B., Roush, T. L., Owen, T. C., Quirico, E., Geballe, T. R., de Bergh, C., Bartholomew, M. J., Dalle Ore, C. M., Doute, S., and Meier, R. (2000). Water ice on Triton. *Icarus*, **147**, 309–316.

Crumpler, L. S., Aubele, J. C., Senske, D. A., Keddie, S. T., Magee, K. P., and Head, J. W. (1997). Volcanoes and centers of volcanism on Venus. In *Venus II: Geology, Geophysics, Atmosphere, and Solar Wind Environment*, eds. S. W. Bougher, D. M. Hunten and R. J. Phillips. Tucson, AZ: University of Arizona Press, pp. 697–756.

Davies, M. E. and Batson, R. M. (1975). Surface coordinates and cartography of Mercury. *J. Geophys. Res.*, **80**, 2417–2430.

Davies, M. E., Dwornik, S. E., Gault, D. E., and Strom, R. G. (1978). *Atlas of Mercury*, NASA Spec. Publ. SP-423.

Davis, P. A. and Soderblom, L. A. (1984). Modeling crater topography and albedo from monoscopic Viking Orbiter images: I. Methodology. *J. Geophys. Res.*, **89**, 9449–9457.

Davis, P. A., Tanaka, K. L., and Golombek, M. P. (1995). Topography of closed depressions, scarps, and grabens in the north Tharsis region of Mars: Implications for shallow crustal discontinuities and graben formation. *Icarus*, **114**, 403–422.

Dimitrova, L. L., Holt, W. E., Haines, A. J., and Schultz, R. A. (2006). Towards understanding the history and mechanisms of Martian faulting: The contribution of gravitational potential energy. *Geophys. Res. Lett.*, **33**, doi:10.1029/2005GL025307.

Dohm, J. M. and Tanaka, K. L. (1999). Geology of the Thaumasia region, Mars: Plateau development, valley origins, and magmatic evolution. *Planet. Space Sci.*, **47**, 411–431.

Dohm, J. M., Tanaka, K. L., and Hare, T. M. (2001a). Geologic map of the Thaumasia region of Mars. U.S. Geol. Surv. Misc. Invest. Ser. Map I-2650, scale 1:5 000 000.

Dohm, J. M., Ferris, J. C., Baker, V. R., Anderson, R. C., Hare, T. M., Strom, R. G., Barlow, N. G., Tanaka, K. L., Klemaszewski, J. E., and Scott, D. H. (2001b). Ancient drainage basin of the Tharsis region, Mars: Potential source for outflow channel systems and putative oceans or paleolakes. *J. Geophys. Res.*, **106**, 32 943–32 958.

Dohm, J. M., Baker, V. R., Maruyama, S., and Anderson, R. C. (2007a). Traits and evolution of the Tharsis superplume, Mars. In *Superplumes: Beyond Plate Tectonics*, eds. D. A. Yuen, S. Maruyama, S.-I. Karato and B. F. Windley. London: Springer, pp. 523–537.

Dohm, J. M., Barlow, N. G., Anderson, R. C., Williams, J.-P., Miyamoto, H., Ferris, J. C., Strom, R. G., Taylor, G. J., Fairén, A. G., Baker, V. R., Boynton, W. V., Keller, J. M., Kerry, K., Janes, D., Rodríguez, A., and Hare, T. M. (2007b). Possible ancient giant basin and related water enrichment in the Arabia Terra province, Mars. *Icarus*, doi:10.1016/j.Icarus.2007.03.006.

Dombard, A. J. and McKinnon, W. B. (2001). Formation of grooved terrain on Ganymede: Extensional instability mediated by cold, superplastic creep. *Icarus*, **154**, 321–336.

Downs, G. S., Mouginis-Mark, P. J., Zisk, S. H., and Thompson, T. W. (1982). New radar derived topography for the northern hemisphere of Mars. *J. Geophys. Res.*, **87**, 9747–9754.

Elachi, C., Wall, S., Allison, M., Anderson, Y., Boehmer, R., Callahan, P., Encrenaz, P., Flamini, E., Franceschetti, G., Gim, Y., Hamilton, G., Hensley, S., Janssen, M., Johnson, W., Kelleher, K. *et al.* (2005). Cassini radar views the surface of Titan. *Science*, **308**, 970–974.

Fairén, A. G. and Dohm, J. M. (2004). Age and origin of the lowlands of Mars. *Icarus*, **168**, 277–284.

Ferrill, D. A., Wyrick, D. Y., Morris, A. P., Sims, D. W., and Franklin, N. M. (2004). Dilational fault slip and pit chain formation on Mars. *GSA Today*, **14**, 4–12.

Figueredo, P. H. and Greeley, R. (2004). Resurfacing history of Europa from pole-to-pole geological mapping. *Icarus*, **167**, 287–312.

Ford, P. G. and Pettengill, G. H. (1992). Venus topography and kilometer-scale slopes. *J. Geophys. Res.*, **97**, 13 103–13 114.

Ford, J. P., Blom, R. G., Crisp, J. A., Elachi, C., Farr, T. G., Saunders, R. S., Theilig, E. E., Wall, S. D., and Yewell, S. B. (1989). *Spaceborne Radar Observations: A Guide for Magellan Radar-Image Analysis*. JPL Publ. 89–41. Pasadena, CA: Jet Propulsion Laboratory, 126pp.

Ford, J. P., Plaut, J. J., Weitz, C. M., Farr, T. G., Senske, D. A., Stofan, E. R., Michaels, G., and Parker, T. J. (1993). *Guide to Magellan Image Interpretation*. JPL Publ. 93–24. Pasadena, CA: Jet Propulsion Laboratory, 148pp.

Forsythe, R. D. and Zimbelman, J. R. (1988). Is the Gordii Dorsum escarpment on Mars an exhumed transcurrent fault? *Nature*, **336**, 143–146.

Frey, H. V. (2006). Impact constraints on, and a chronology for, major events in early Mars history. *J. Geophys. Res.*, **111**, doi:10.1029/2005JE002449.

Frey, H., Roark, J. H., Shockey, K. M., Frey, E. L., and Sakimoto, S. H. E. (2002). Ancient lowlands on Mars. *Geophys. Res. Lett.*, **29**, 1384, doi:10.1029/2001GL013832.

Furfaro, R., Dohm, J. M., Fink, W., Kargel, J. S., Schulze-Makuch, D., Fairén, A. G., Ferre, P. T., Palmero-Rodriguez, A., Baker, V. R., Hare, T. M., Tarbell, M., Miyamoto, H. H., and Komatsu, G. (2007). The search for life beyond Earth through fuzzy expert systems. *Planet. Space Sci.*, **56**, 448–472.

Ghent, R. R. and Hansen, V. L. (1999). Structural and kinematic analysis of eastern Ovda Regio, Venus: Implications for crustal plateau formation. *Icarus*, **139**, 116–136.

Gilbert, G. K. (1886). The inculcation of scientific method by example, with an illustration drawn from the Quaternary of Utah. *Am. J. Sci.*, **31** (3rd Series), 284–299.

Gilbert, G. K. (1893). The Moon's face, a study of the origin of its features. *Philos. Soc. Wash. Bull.*, **12**, 241–292.

Gilmore, M. S., Collins, G. C., Ivanov, M. A., Marinangeli, L., and Head, J. W. (1998). Style and sequence of extensional structures in tessera terrain, Venus. *J. Geophys. Res.*, **103**, 16 813–16 840.

Golombek, M. P. (1979). Structural analysis of lunar grabens and the shallow crustal structure of the Moon. *J. Geophys. Res.*, **84**, 4657–4666.

Golombek, M. P. (1982). Constraints on the expansion of Ganymede and the thickness of the lithosphere (abs.). *Proc. Lunar Planet. Sci. Conf.* 13. *J. Geophys. Res.*, **87**, A77–A83.

Golombek, M. P. (1992). Planetary tectonic processes, terrestrial planets. In *The Astronomy and Astrophysics Encyclopedia*, ed. S. P. Maran. New York: Van Nostrand Reinhold, pp. 544–546.

Golombek, M. P. and McGill, G. E. (1983). Grabens, basin tectonics, and the maximum total expansion of the Moon. *J. Geophys. Res.*, **88**, 3563–3578.

Golombek, M. P., Plescia, J. B., and Franklin, B. J. (1991). Faulting and folding in the formation of planetary wrinkle ridges. *Proc. Lunar Planet. Sci. Conf. 21*, 679–693.

Golombek, M. P., Tanaka, K. L., and Franklin, B. J. (1996). Extension across Tempe Terra, Mars, from measurements of fault scarp widths and deformed craters. *J. Geophys. Res.*, **101**, 26 119–26 130.

Golombek, M. P., Anderson, F. S., and Zuber, M. T. (2001). Martian wrinkle ridge topography: Evidence for subsurface faults from MOLA. *J. Geophys. Res.*, **106**, 23 811–23 821.

Gomes, R., Levison, H. F., Tsiganis, K., and Morbidelli, A. (2005). Origin of the cataclysmic late heavy bombardment period of the terrestrial planets. *Nature*, **435**, 466–469.

Goudy, C. L. and Schultz, R. A. (2005). Dike intrusions beneath grabens south of Arsia Mons, Mars. *Geophys. Res. Lett.*, **32**, doi:10.1029/2004GL021977.

Goudy, C. L., Schultz, R. A., and Gregg, T. K. P. (2005). Coulomb stress changes in Hesperia Planum, Mars, reveal regional thrust fault reactivation. *J. Geophys. Res.*, **110**, doi:10.1029/2004JE002293.

Greeley, R. and Guest, J. E. (1987). Geologic map of the eastern equatorial region of Mars. U.S. Geol. Surv. Misc. Invest. Ser., Map I-1802-B, scale 1:15 000 000.

Greeley, R., Chyba, C., Head, J. W., McCord, T., McKinnon, W. B., and Pappalardo, R. T. (2004). Geology of Europa. In *Jupiter: The Planet, Satellites and Magnetosphere*, eds. F. Bagenal, T. E. Dowling and W. B. McKinnon. Tucson, AZ: University of Arizona Press, pp. 329–362.

Greenberg, R., Croft, S. K., Janes, D. M., Kargel, J. S., Lebofsky, L. A., Lunine, J. I., Marcialis, R. L., Melosh, H. J., Ojakangas, G. W., and Strom, R. G. (1991). Miranda. In *Uranus*, eds. J. T. Bergstralh *et al.* Tucson, AZ: University of Arizona Press, pp. 693–735.

Greenberg, R., Geissler, P. E., Hoppa, G., Tufts, B. R., Durda, D. D., Pappalardo, R., Head, J. W., Greeley, R., Sullivan, R., and Carr, M. H. (1998). Tectonic processes on Europa: Tidal stresses, mechanical response, and visible features. *Icarus*, **135**, 64–78.

Greenberg, R., Hoppa, G. V., Tufts, B. R., Geissler, P. E., and Reilly, J. (1999). Chaos on Europa. *Icarus*, **141**, 263–286.

Guest, J. E. and Stofan, E. R. (1999). A new view of the stratigraphic history of Venus. *Icarus*, **139**, 55–66.

Guest, J. E., Bulmer, M. H., Aubele, J. C., Beratan, K., Greeley, R., Head, J. W., Michaels, G., Weitz, C., and Wiles, C. (1992). Small volcanic edifices and volcanism in the plains on Venus. *J. Geophys. Res.*, **97**, 15 949–15 966.

Hansen, V. L. (2000). Geologic mapping of tectonic planets. *Earth Planet. Sci. Lett.*, **176**, 527–542.

Hansen, V. L. (2005). Venus's shield terrain. *Geol. Soc. Am. Bull.*, **117**, 808–822.

Hansen, V. L. (2006). Geologic constraints on crustal plateau surface histories, Venus: The lava pond and bolide impact hypotheses. *J. Geophys. Res.*, **111**, doi:10.1029/2006JE002714.

Hansen, V. L. and Willis, J. J. (1996). Structural analysis of a sampling of tesserae: Implications for Venus geodynamics. *Icarus*, **123**, 296–312.

Hansen, V. L. and Willis, J. J. (1998). Ribbon terrain formation, southwestern Fortuna Tessera, Venus: Implications for lithosphere evolution. *Icarus*, **132**, 321–343.

Hansen, V. L., Banks, B. K., and Ghent, R. R. (1999). Tessera terrain and crustal plateaus, Venus. *Geology*, **27**, 1071–1074.

Hansen, V. L., Phillips, R. J., Willis, J. J., and Ghent, R. R. (2000). Structures in tessera terrain, Venus: Issues and answers. *J. Geophys. Res.*, **105**, 4135–4152.

Hapke, B., Danielson, E., Klaasen, K., and Wilson, L. (1975). Photometric observations of Mercury from Mariner 10. *J. Geophys. Res.*, **80**, 2431–2443.

Harmon, J. K., Campbell, D. B., Bindschadler, K. L., Head, J. W., and Shapiro, I. I. (1986). Radar altimetry of Mercury: A preliminary analysis. *J. Geophys. Res.*, **91**, 385–401.

Hartmann, W. K. and Neukum, G. (2001). Cratering chronology and evolution of Mars. *Space Sci. Rev.*, **96**, 165–194.

Hauber, E. and Kronberg, P. (2005). The large Thaumasia graben on Mars: Is it a rift? *J. Geophys. Res.*, **110**, doi:10.1029/2005JE002407.

Hauck, S. A., Dombard, A. J., Phillips, R. J., and Solomon, S. C. (2004). Internal and tectonic evolution of Mercury. *Earth Planet. Sci. Lett.*, **222**, 713–728.

Head, J. W., Kreslavsky, M. A., and Pratt, S. (2002). Northern lowlands of Mars: Evidence for widespread volcanic flooding and tectonic deformation in the Hesperian period. *J. Geophys. Res.*, **107**, doi:10.1029/2000JE001445.

Helfenstein, P., Thomas, P. C., and Veverka, J. (1989). Evidence from Voyager II photometry for early resurfacing of Umbriel. *Nature*, **338**, 324–326.

Herrick, R. R. and Sharpton, V. L. (2000). Implications from stereo-derived topography of Venusian impact craters. *J. Geophys. Res.*, **105**, 20 245–20 262.

Herrick, R. R., Sharpton, V. L., Malin, M. C., Lyons, S. N., and Feely, K. (1997). Morphology and morphometry of impact craters. In *Venus II: Geology, Geophysics, Atmosphere, and Solar Wind Environment*, eds. S. W. Bougher, D. M. Hunten and R. J. Phillips. Tucson, AZ: University of Arizona Press, pp. 1015–1046.

Hillier, J. and Squyres, S. W. (1991). Thermal stress tectonics on the satellites of Saturn and Uranus. *J. Geophys. Res.*, **96**, 15 665–15 674.

Hoppa, G. V., Tufts, B. R., Greenberg, R., and Geissler, P. E. (1999a). Formation of cycloidal features on Europa. *Science*, **285**, 1899–1902.

Hoppa, G., Tufts, B. R., Greenberg, R., and Geissler, P. (1999b). Strike-slip faults on Europa: Global shear patterns driven by tidal stress. *Icarus*, **141**, 287–298.

Howard, K. A. and Muehlberger, W. R. (1973). Lunar thrust faults in the Taurus-Littrow region. In *Apollo 17 Prel. Sci. Rep.*, NASA SP-330, 31–12 to 31–21.

Hurford, T. A., Helfenstein, P., Hoppa, G. V., Greenberg, R., and Bills, B. G. (2007). Eruptions arising from tidally controlled periodic openings of rifts on Enceladus. *Nature*, **447**, 292–294.

Hussmann, H. and Spohn, T. (2004). Coupled thermal and orbital evolution of Europa and Io. *Icarus*, **171**, 391–410.

Ivanov, M. A. and Head, J. W. (1996). Tessera terrain on Venus: A survey of the global distribution, characteristics, and relation to surrounding units from Magellan data. *J. Geophys. Res.*, **101**, 14 861–14 908.

Jaeger, W. L., Turtle, E. P., Keszthelyi, L. P., Radebaugh, J., McEwen, A. S., and Pappalardo, R. T. (2003). Orogenic tectonism on Io. *J. Geophys. Res.*, **108**, doi:10.1029/2002JE001946.

Janes, D. M. and Melosh, H. J. (1988). Sinker tectonics: An approach to the surface of Miranda. *J. Geophys. Res.*, **93**, 3127–3143.

Jankowski, D. J. and Squyres, S. W. (1988). Solid-state ice volcanism on the satellites of Uranus. *Science*, **241**, 1322–1325.

Johnson, T. V. (2005). Geology of the icy satellites. *Space Sci. Rev.*, **116**, 401–420.

King, S. D. (2008). Pattern of lobate scarps on Mercury's surface reproduced by a model of mantle convection. *Nature Geosciences*, **1**, 229–232.

Kirk, R. L., Soderblom, L. A., and Lee, E. L. (1992). Enhanced visualization for interpretation of Magellan radar data: Supplement to the Magellan Special Issue. *J. Geophys. Res.*, **97**, 16 371–16 381.

Kirk, R. L., Howington-Kraus, E., Redding, B., Galuszka, D., Hare, T. M., Archinal, B. A., Soderblom, L. A., and Barrett, J. M. (2003). High-resolution topomapping of candidate MER landing sites with Mars Orbiter Camera narrow-angle images. *J. Geophys. Res.*, **108**, doi:10.1029/2003JE002131.

Kivelson, M. G., Khurana, K. K., Stevenson, D. J., Bennett, L., Joy, S., Russell, C. T., Walker, R. J., Zimmer, C., and Polanskey, C. (1999). Europa and Callisto: Induced or intrinsic fields in a periodically varying plasma environment. *J. Geophys. Res.*, **104**, 4609–4625.

Kivelson, M. G., Khurana, K. K., and Volwerk, M. (2002). The permanent and inductive magnetic moments of Ganymede. *Icarus*, **157**, 507–522.

Knapmeyer, M., Oberst, J., Hauber, E., Wählisch, M., Deuchler, C., and Wagner, R. (2006). Working models for spatial distribution and level of Mars' seismicity. *J. Geophys. Res.*, **111**, E11006, doi:10.1029/2006JE002708.

Koenig, E. and Aydin, A. (1998). Evidence for large-scale strike-slip faulting on Venus. *Geology*, **26**, 551–554.

Komatsu, G., Gulick, V. C., and Baker, V. R. (2001). Valley networks on Venus. *Geomorphology*, **37**, 225–240.

Kring, D. A. and Cohen, B. A. (2002). Cataclysmic bombardment throughout the inner solar system 3.9–4.0 Ga. *J. Geophys. Res.*, **107**, doi:10.1029/2001JE001529.

Kumar, P. S. (2005). An alternative kinematic interpretation of Thetis Boundary Shear Zone, Venus: Evidence for strike-slip ductile duplexes. *J. Geophys. Res.*, **110**, doi:10.1029/2004JE002387.

Lillesand, T. M. and Kiefer, R. W. (1994). *Remote Sensing and Image Interpretation*, 3rd edn. New York: John Wiley & Sons.

Lucchitta, B. K. (1976). Mare ridges and highland scarps: Results of vertical tectonism? *Proc. Lunar Sci. Conf. 7*, 2761–2782.

Lucchitta, B. K. (1977). Topography, structure, and mare ridges in southern Mare Imbrium and northern Oceanus Procellarum. *Proc. Lunar Sci. Conf. 8*, 2691–2703.

Lucchitta, B. K., McEwen, A. S., Clow, C. D., Geissler, R. B., Singer, R. B., Schultz, R. A., and Squyres, S. W. (1992). The canyon system on Mars. In *Mars*, eds. H. H. Kieffer, B. M. Jakosky, C. W. Snyder and M. S. Matthews. Tucson, AZ: University of Arizona Press, pp. 453–492.

Margot, J. L., Campbell, D. B., Jurgens, R. F., and Slade, M. A. (1999). Topography of the lunar poles from radar interferometry: A survey of cold trap locations. *Science*, **284**, 1658–1660.

Márquez, A., Fernández, C., Anguita, F., Farelo, A., Anguita, J., and de la Casa, M.-A. (2004). New evidence for a volcanically, tectonically, and climatically active Mars. *Icarus*, **172**, 573–581.

Masursky, H., Colton, G. W., and El-Baz, F. (eds.) (1978). *Apollo Over the Moon: A View From Orbit*, NASA SP-362. Washington, DC: NASA Scientific and Technical Information Office.

Maxwell, T. A., El-Baz, F., and Ward, S. H. (1975). Distribution, morphology, and origin of ridges and arches in Mare Serenitatis. *Geol. Soc. Am. Bull.*, **86**, 1273–1278.

McEwen, A. S., Kezthelyi, L., Lopes, R., Schenk, P., and Spencer, J. (2004). The lithosphere and surface of Io. In *Jupiter: The Planet, Satellites and Magnetosphere*, eds. F. Bagenal, T. E. Dowling and W. B. McKinnon. Tucson, AZ: University of Arizona Press, pp. 307–328.

McGill, G. E. (1971). Attitude of fractures bounding straight and arcuate lunar rilles. *Icarus*, **14**, 53–58.

McGill, G. E. (1986). The giant polygons of Utopia, northern Martian plains. *Geophys. Res. Lett.*, **13**, 705–708.

McGill, G. E. (1989). Buried topography of Utopia, Mars: Persistence of a giant impact depression. *J. Geophys. Res.*, **94**, 2753–2759.

McGill, G. E. and Hills, L. S. (1992). Origin of giant Martian polygons. *J. Geophys. Res.*, **97**, 2633–2647.

McKinnon, W. B. (1982). Tectonic deformation of Galileo Regio and limits to the planetary expansion of Ganymede. *Proc. Lunar Planet. Sci. Conf. 12*, 1585–1597.

McKinnon, W. B. and Melosh, H. J. (1980). Evolution of planetary lithospheres: Evidence from multiring basins on Ganymede and Callisto. *Icarus*, **44**, 454–471.

Mége, D. and Masson, P. (1996). Amounts of crustal stretching in Valles Marineris, Mars. *Planet. Space Sci.*, **44**, 749–781.
Melosh, H. J. (1976). On the origin of fractures radial to lunar basins. *Proc. Lunar Sci. Conf. 7*, 2967–2982.
Melosh, H. J. (1978). The tectonics of mascon loading. *Proc. Lunar Planet. Sci. Conf. 9*, 3513–3525.
Melosh, H. J. (1989). *Impact Cratering: A Geologic Process.* New York: Oxford University Press.
Melosh, H. J. and Dzurisin, D. (1978a). Tectonic implications for gravity structure of Caloris basin, Mercury. *Icarus*, **33**, 141–144.
Melosh, H. J. and Dzurisin, D. (1978b). Mercurian global tectonics: A consequence of tidal despinning? *Icarus*, **35**, 227–236.
Melosh, H. J. and McKinnon, W. B. (1988). The tectonics of Mercury. In *Mercury*, eds. F. Vilas, C. R. Chapman and M. S. Matthews. Tucson, AZ: University of Arizona Press, pp. 374–400.
Moore, J. M. (1984). The tectonic and volcanic history of Dione. *Icarus*, **59**, 205–220.
Moore, J. M. and Ahern, J. L. (1983). The geology of Tethys. *J. Geophys. Res.*, **88**, A577–A584.
Moore, J. M., Sullivan, R. J., Chuang, F. C., Head, J. W., McEwen, A. S., Milazzo, M. P., Nixon, B. E., Pappalardo, R. T., Schenk, P. M., and Turtle, E. P. (2001). Landform degradation and slope processes on Io: The Galileo view. *J. Geophys. Res.*, **106**, 33 223–33 240.
Moore, J. M., Chapman, C. R., Chapman., C., Bierhaus, E., Greeley, R., Chuang, F., Klemaszewski, J., Clark, R., Dalton, J., Hibbitts, C., Schenk, P., Spencer, J., and Wagner, R. (2004a). Callisto. In *Jupiter: The Planet, Satellites and Magnetosphere*, eds. F. Bagenal, T. E. Dowling and W. B. McKinnon. Tucson, AZ: University of Arizona Press, pp. 397–426.
Moore, J. M., Schenk, P. M., Bruesch, L. S., Asphaug, E., and McKinnon, W. B. (2004b). Large impact features on middle-sized icy satellites. *Icarus*, **171**, 421–443.
Moore, W. B. (2006). Thermal equilibrium in Europa's ice shell. *Icarus*, **180**, 141–146.
Moore, W. B. and Schubert, G. (2000). The tidal response of Europa. *Icarus*, **147**, 317–319.
Montesi, L. G. J. and Zuber, M. T. (2003a). Spacing of faults at the scale of the lithosphere and localization instability: 1. Theory. *J. Geophys. Res.*, **108**, doi:10.1029/2002JB001923.
Montesi, L. G. J. and Zuber, M. T. (2003b). Clues to the lithospheric structure of Mars from wrinkle ridge sets and localization instability. *J. Geophys. Res.*, **108**, doi:10.1029/2002JE001974.
Murchie, S. L. and Head, J. W. (1988). Possible breakup of dark terrain on Ganymede by large-scale shear faulting. *J. Geophys. Res.*, **93**, 8795–8824.
Murchie, S. L., Watters, T. R., Robinson, M. S., Head, J. W., Strom, R. G., Chapman, C. R., Solomon, S. C., McClintock, W. E., Prockter, L. M., Domingue, D. L., and Blewett, D. T. (2008). Geology of the Caloris Basin, Mercury: A new view from MESSENGER. *Science*, **321**, 73–76.
Nimmo, F. and Giese, B. (2005). Thermal and topographic tests of Europa chaos formation models from Galileo E15 observations. *Icarus*, **177**, 327–340.
Nimmo, F. and Pappalardo, R. T. (2006). Diapir-induced reorientation of Saturn's moon Enceladus. *Nature*, **441**, 614–616.
Nimmo, F. and Tanaka, K. (2005). Early crustal evolution of Mars. *Annu. Rev. Earth Planet. Sci.*, **33**, 133–161.

Nimmo, F., Spencer, J. R., Pappalardo, R. T., and Mullen, M. E. (2007). Shear heating as the origin of the plumes and heat flux on Enceladus. *Nature*, **447**, 289–291.

Ojakangas, G. W. and Stevenson, D. J. (1989). Thermal state of an ice shell on Europa. *Icarus*, **81**, 220–241.

Okubo, C. H. and Martel, S. J. (1998). Pit crater formation on Kilauea volcano, Hawaii. *J. Volcan. Geotherm. Res.*, **86**, 1–18.

Okubo, C. H. and Schultz, R. A. (2003). Thrust fault vergence directions on Mars: A foundation for investigating global-scale Tharsis-driven tectonics. *Geophys. Res. Lett.*, **30**, doi:10.1029/2003GL018664.

Okubo, C. H. and Schultz, R. A. (2004). Mechanical stratigraphy in the western equatorial region of Mars based on thrust fault-related fold topography and implications for near-surface volatile reservoirs. *Geol. Soc. Am. Bull*, **116**, 594–605.

Okubo, C. H. and Schultz, R. A. (2006). Variability in Early Amazonian Tharsis stress state based on wrinkle ridges and strike-slip faulting. *J. Struct. Geol.*, **28**, 2169–2181.

Okubo, C. H., Schultz, R. A., and Stefanelli, G. S. (2004). Gridding Mars Orbiter Laser Altimeter data with GMT: Effects of pixel size and interpolation methods on DEM integrity. *Computers Geosci.*, **30**, 59–72.

Pappalardo, R. T. and Collins, G. C. (2005). Strained craters on Ganymede. *J. Struct. Geol.*, **27**, 827–838.

Pappalardo, R. T., Reynolds, S. J., and Greeley, R. (1997). Extensional tilt blocks on Miranda: Evidence for an upwelling origin of Arden Corona. *J. Geophys. Res.*, **102**, 13 369–13 379.

Pappalardo, R. T. *et al.* (1999). Does Europa have a subsurface ocean? Evaluation of the geological evidence. *J. Geophys. Res.*, **104**, 24 015–24 055.

Pappalardo, R. T., Collins, G. C., Head, J. W., Helfenstein, P., McCord, T., Moore, J. M., Prockter, L. M., Schenk, P. M., and Spencer, J. R. (2004). Geology of Ganymede. In *Jupiter: The Planet, Satellites and Magnetosphere*, eds. F. Bagenal, T. E. Dowling and W. B. McKinnon. Tucson, AZ: University of Arizona Press, pp. 363–396.

Pechmann, J. C. (1980). The origin of polygonal troughs on the northern plains of Mars. *Icarus*, **42**, 185–210.

Pechmann, J. B. and Melosh, H. J. (1979). Global fracture patterns of a despun planet application to Mercury. *Icarus*, **38**, 243–250.

Pettengill, G. H., Eliason, E., Ford, P. G., Loriot, G. B., Masursky, H., and McGill, G. E. (1980). Pioneer Venus radar results: Altimetry and surface properties. *J. Geophys. Res.*, **85**, 8261–8270.

Phillips, R. J. and Hansen, V. L. (1994). Tectonic and magmatic evolution of Venus. *Annu. Rev. Earth Planet. Sci.*, **22**, 597–654.

Phillips, R. J. and Hansen, V. L. (1998). Geological evolution of Venus: Rises, plains, plumes, and plateaus. *Science*, **279**, 1492–1497.

Phillips, R. J. and Solomon, S. C. (1997). Compressional strain history of Mercury (abs.). *Lunar Planet. Sci. Conf. XXVIII*, 1107–1108.

Phillips, R. J., Raubertas, R. F., Arvidson, R. E., Sarkar, I. C., Herrick, R. R., Izenberg, N., and Grimm, R. E. (1992). Impact craters and Venus resurfacing history. *J. Geophys. Res.*, **97**, 15 923–15 948.

Phillips, R. J., Zuber, M. T., Solomon, S. C., Golombek, M. P., Jakosky, B. M., Banerdt, W. B., Smith, D. E., Williams, R. M. E., Hynek, B. M., Aharonson, O., and Hauck II, S. A. (2001). Ancient geodynamics and global-scale hydrology on Mars. *Science*, **291**, 2587–2591.

Plaut, J. J. (1993). Stereo imaging. In *Guide to Magellan Image Interpretation*, eds. J. P. Ford, J. J. Plaut, C. M. Weitz, T. G. Farr, D. A. Senske, E. R. Stofan, G. Michaels and

T. J. Parker. JPL Publ. 93–24. Pasadena, CA: NASA and Jet Propulsion Laboratory, pp. 33–37.

Plescia, J. B. (1987). Geologic terrains and crater frequencies on Ariel. *Nature*, **327**, 201–204.

Plescia, J. B. (1988). Cratering history of Miranda: Implications for geologic processes. *Icarus*, **73**, 442–461.

Plescia, J. B. and Golombek, M. P. (1986). Origin of planetary wrinkle ridges based on the study of terrestrial analogs. *Geol. Soc. Am. Bull.*, **97**, 1289–1299.

Plescia, J. B. and Saunders, R. S. (1982). Tectonic history of the Tharsis Region, Mars. *J. Geophys. Res.*, **87**, 9775–9791.

Polit, A. T. (2005). Influence of mechanical stratigraphy and strain on the displacement–length scaling of normal faults on Mars, 2005. M.S. thesis, University of Nevada, Reno.

Porco, C. C., Baker, E., Barbara, J., Beurle, K., Brahic, A., Burns, J. A., Charnoz, S., Cooper, N., Dawson, D. D., Del Genio, A. D., Tilmann, D., Dones, L., Dyudina, U., Evans, M. W., Fussner, S. *et al.* (2005a). Imaging of Titan from the Cassini spacecraft. *Nature*, **434**, 159.

Porco, C. C., Baker, E., Barbara, J., Beurle, K., Brahic, A., Burns, J. A., Charnoz, S., Cooper, N., Dawson, D. D., Del Genio, A. D., Denk, T., Dones, L., Dyudina, U., Evans, M. W., Giese, B. *et al.* (2005b). Cassini imaging science: Initial results on Phoebe and Iapetus. *Science*, **307**, 1237–1242.

Porco C. C., Helfenstein, P., Thomas, P. C., Ingersoll, A. P., Wisdom, J., West, R., Neukum, G., Denk, T., Wagner, R., Roatsch, T., Kieffer, S., Turtle, E., McEwen, A., Johnson, T. B., Rathbun, J. *et al.* (2006). Cassini observes the active south pole of Enceladus. *Science*, **311**, 1393–1401.

Price, M. and Suppe, J. (1995). Constraints on the resurfacing history of Venus from the hypsometry and distribution of volcanism, tectonism, and impact craters. *Earth, Moon and Planets*, **71**, 99–145.

Prockter, L. M., Head, J. W., Pappalardo, R. T., Sullivan, R. L., Clifton, A. E., Giese, B., Wagner, R., and Neukum, G. (2002). Morphology of Europan bands at high resolution: A mid-ocean ridge-type rift mechanism. *J. Geophys. Res.*, **107**, doi:10.1029/2000JE001458.

Prockter, L. M., Pappalardo, R. T., and Nimmo, F. (2005). A shear heating origin for ridges on Triton. *Geophys. Res. Lett.*, **32**, doi:10.1029/2005GL022832.

Riley, J., Hoppa, G. V., Greenberg, R., Tufts, B. R., and Geissler, P. (2000). Distribution of chaotic terrain on Europa. *J. Geophys. Res.*, **105**, 22 599–22 615.

Robinson, M. S., Davies, M. E., Colvin, T. R., and Edwards, K. E. (1999). A revised control network for Mercury. *J. Geophys. Res.*, **104**, 30 847–30 852.

Sabins, F. F. (1997). *Remote Sensing: Principles and Interpretation.* New York: W.H. Freeman and Company.

Schaber, G. G. and McCauley, J. F. (1980). Geologic map of the Tolstoj quadrangle of Mercury. U.S. Geol. Surv. Misc. Invest. Ser., Map I-1199, scale 1:5 000 000.

Schaber, G. G., Strom, R. G., Moore, H. J., Soderblom, L. A., Kirk, R. L., Chadwick, D. J., Dawson, D. D., Gaddis, L. A., Boyce, J. M., and Russell, J. (1992). Geology and distribution of impact craters on Venus: What are they telling us? *J. Geophys. Res.*, **97**, 13 257–13 302.

Schenk, P. M. (1991). Fluid volcanism on Miranda and Ariel: Flow morphology and composition. *J. Geophys. Res.*, **96**, 1887–1906.

Schenk, P. M. (1993). Central pit and dome craters: Exposing the interiors of Ganymede and Callisto. *J. Geophys. Res.*, **98**, 7475–7498.

Schenk, P. M. and Bulmer, M. H. (1998). Origin of mountains on Io by thrust faulting and large-scale mass movements. *Science*, **279**, 1514–1517.
Schenk, P. M. and Bussey, D. B. J. (2004). Galileo stereo topography of the lunar north polar region. *Geophys. Res. Lett.*, **31**, doi:10.1029/2004GL021197.
Schenk, P. M. and Jackson, M. P. A. (1993). Diapirism on Triton: A record of crustal layering and instability. *Geology*, **21**, 299–302.
Schenk, P. M. and McKinnon, W. B. (1987). Ring geometry on Ganymede and Callisto. *Icarus*, **72**, 209–234.
Schenk, P. M. and McKinnon, W. B. (1989). Fault offsets and lateral crustal movement on Europa: Evidence for a mobile ice shell. *Icarus*, **79**, 75–100.
Schenk, P. M., McKinnon, W. B., Gwynn, D., and Moore, J. M. (2001a). Flooding of Ganymede's bright terrains by low-viscosity water-ice lavas. *Nature*, **410**, 57–60.
Schenk, P., Hargitai, H., Wilson, R., McEwen, A., and Thomas, P. (2001b). The mountains of Io: Global and geological perspectives from Voyager and Galileo. *J. Geophys. Res.*, **106**, 33 201–33 222.
Schenk, P. M., Chapman, C. R., Zahnle, K., and Moore, J. M. (2004). Ages and interiors: The cratering record of the Galilean satellites. In *Jupiter: The Planet, Satellites and Magnetosphere*, eds. F. Bagenal, T. E. Dowling and W. B. McKinnon. Tucson, AZ: University of Arizona Press, pp. 427–456.
Schubert, G., Spohn, T., and Reynolds, R. T. (1986). Thermal histories and internal structures of the moons of the solar system. In *Satellites*, eds. J. A. Burns and M. S. Matthews. Tucson, AZ: University of Arizona Press, pp. 224–292.
Schultz, P. H. (1976). *Moon Morphology.* Austin: University of Texas Press.
Schultz, R. A. (1985). Assessment of global and regional tectonic models for faulting in the ancient terrains of Mars. *J. Geophys. Res.*, **90**, 7849–7860. (Correction to Schultz, R. A. Assessment of global and regional tectonic models for faulting in the ancient terrains of Mars. *J. Geophys. Res.*, **91**, 12 861–12 863, 1986.)
Schultz, R. A. (1989). Strike-slip faulting of ridged plains near Valles Marineris, Mars. *Nature*, **341**, 424–426.
Schultz, R. A. (1991). Structural development of Coprates Chasma and western Ophir Planum. *J. Geophys. Res.*, **96**, 22 777–22 792.
Schultz, R. A. (1995). Gradients in extension and strain at Valles Marineris. *Planet. Space Sci.*, **43**, 1561–1566.
Schultz, R. A. (1998). Multiple-process origin of Valles Marineris basins and troughs. *Planet. Space Sci.*, **46**, 827–834.
Schultz, R. A. (1999). Understanding the process of faulting: Selected challenges and opportunities at the edge of the 21st century. *J. Struct. Geol.*, **21**, 985–993.
Schultz, R. A. (2000a). Localization of bedding-plane slip and backthrust faults above blind faults: Keys to wrinkle ridge structure. *J. Geophys. Res.*, **105**, 12 035–12 052.
Schultz, R. A. (2000b). Fault-population statistics at the Valles Marineris Extensional Province, Mars: Implications for segment linkage, crustal strains, and its geodynamical development. *Tectonophysics*, **316**, 169–193.
Schultz, R. A. and Lin, J. (2001). Three-dimensional normal faulting models of Valles Marineris, Mars, and geodynamic implications. *J. Geophys. Res.*, **106**, 16 549–16 566.
Schultz, R. A. and Tanaka, K. L. (1994). Lithospheric-scale buckling and thrust structures on Mars: The Coprates rise and south Tharsis ridge belt. *J. Geophys. Res.*, **99**, 8371–8385.
Schultz, R. A. and Watters, T. R. (2001). Forward mechanical modeling of the Amenthes Rupes thrust fault on Mars. *Geophys. Res. Lett.*, **28**, 4659–4662.

Schultz, R. A. and Zuber, M. T. (1994). Observations, models, and mechanisms of failure of surface rocks surrounding planetary surface loads. *J. Geophys. Res.*, **99**, 14 691–14 702.

Schultz, R. A., Okubo, C. H., Goudy, C. L., and Wilkins, S. J. (2004). Igneous dikes on Mars revealed by MOLA topography. *Geology*, **32**, 889–892.

Schultz, R. A., Okubo, C. H., and Wilkins, S. J. (2006). Displacement–length scaling relations for faults on the terrestrial planets. *J. Struct. Geol.*, **28**, 2182–2193.

Schultz, R. A., Moore, J. M., Grosfils, E. B., Tanaka, K. L., and Mège, D. (2007). The Canyonlands model for planetary grabens: Revised physical basis and implications. In *The Geology of Mars: Evidence from Earth-Based Analogues*, eds. M. G. Chapman and I. P. Skilling. Cambridge: Cambridge University Press, pp. 371–399.

Schulze-Makuch, D., Dohm, J. M., Fan, C., Fairén, A. G., Rodriguez, J. A. P., Baker, V. R., and Fink, W. (2007). Exploration of hydrothermal targets on Mars. *Icarus*, **189**, 308–324.

Scott, D. H. and Dohm, J. M. (1990). Chronology and global distribution of fault and ridge systems on Mars. *Proc. Lunar Planet. Sci. Conf. 20*, 487–501.

Scott, D. H. and Dohm, J. M. (1997). Mars structural geology and tectonics. In *Encyclopedia of Planetary Sciences*. New York: Van Nostrand Reinhold, pp. 461–463.

Scott, D. H. and Tanaka, K. L. (1986). Geologic map of the western equatorial region of Mars. U.S. Geol. Surv. Misc. Invest. Ser. Map I-1802-A, scale 1:15 000 000.

Sharpton, V. L. and Head, J. W. (1988). Lunar mare ridges: Analysis of ridge-crater intersections and implications for the tectonic origin of mare ridges. *Proc. Lunar Planet. Sci. Conf. 18*, 307–317.

Shoemaker, E. M. and Hackman, R. J. (1962). Stratigraphic basis for a lunar timescale. In *The Moon*, eds. Z. Kopal and Z. K. Mikhailov. London: Academic Press, pp. 289–300.

Shoemaker, E. M., Lucchitta, B. K., Plescia, J. B., Squyres, S. W., and Wilhelms, D. E. (1982). The geology of Ganymede. In *Satellites of Jupiter*, ed. D. Morrison. Tucson, AZ: University of Arizona Press, pp. 435–520.

Simons, M., Solomon, S. C., and Hager, B. H. (1997). Localization of gravity and topography: Constraints on the tectonics and mantle dynamics of Venus. *Geophys. J. Int.*, **131**, 24–44.

Smith, D. E., Zuber, M. T., Solomon, S. C., Phillips, R. J., Head, J. W., Garvin, J. B., Banerdt, W. B., Muhleman, D. O., Pettingill, G. H., Neumann, G. A., Lemoine, F. G., Abshire, J. B., Aharonson, O., Brown, C. D., Hauck, S. A., II *et al.* (1999). The global topography of Mars and implications for surface evolution. *Science*, **284**, 1495–1503.

Smith, D. E., Zuber, M. T., Frey, H. V., Garvin, J. B., Head, J. W., Muhleman, D. O., Pettingill, G. H., Phillips, R. J., Solomon, S. C., Zwally, H. J., Banerdt, W. B., Duxbury, T. C., Golombek, M. P., Lemoine, F. G., Neumann, G. A., *et al.* (2001). Mars Orbiter Laser Altimeter (MOLA): Experiment summary after the first year of global mapping of Mars. *J. Geophys. Res.*, **106**, 23 689–23 722.

Smith-Konter, B. and Pappalardo, R. T. (2008). Tidally driven stress accumulation and shear failure of Enceladus's tiger stripes. *Icarus*, **198**, 435–451.

Solomon, S. C. (1976). Some aspects of core formation in Mercury. *Icarus*, **28**, 509–521.

Solomon, S. C. (1977). The relationship between crustal tectonics and internal evolution in the Moon and Mercury. *Phys. Earth Planet. Inter.*, **15**, 135–145.

Solomon, S. C. (1978). On volcanism and thermal tectonics on one-plate planets. *Geophys. Res. Lett.*, **5**, 461–464.

Solomon, S. C. (1979). Formation, history and energetics of cores in the terrestrial planets. *Phys. Earth Planet. Inter.*, **19**, 168–182.

Solomon, S. C. and Head, J. W. (1979). Vertical movements in mare basins: Relation to mare emplacement, basin tectonics, and lunar thermal history. *J. Geophys. Res.*, **84**, 1667–1682.

Solomon, S. C. and Head, J. W. (1980). Lunar mascon basins: Lava filling, tectonics, and evolution of the lithosphere. *Rev. Geophys.*, **18**, 107–141.

Solomon, S. C. and Head, J. W. (1982). Evolution of the Tharsis province of Mars: The importance of heterogeneous lithospheric thickness and volcanic construction. *J. Geophys. Res.*, **87**, 9755–9774.

Solomon, S. C., Smrekar, S. E., Bindschadler, D. L., Grimm, R. E., Kaula, W. M., McGill, G. E., Phillips, R. J., Saunders, R. S., Schubert, G., Squyres, S. W., and Stofan, E. R. (1992). Venus tectonics: An overview of Magellan observations. *J. Geophys. Res.*, **97**, 13 199–13 255.

Solomon, S. C., McNutt, R. L., Gold, R. E., Acuña, M. H., Baker, D. N., Boynton, W. V., Chapman, C. R., Cheng, A. F., Gloeckler, G., Head, J. W., Krimigis, S. M., McClintock, W. E., Murchie, S. L., Peale, S. J., Philips, R. J., Robinson, M. S., Slavin, J. A., Smith, D. E., Strom, R. G., Trombka, J. I., and Zuber, M. T. (2001). The MESSENGER Mission to Mercury: Scientific objectives and implementation. *Planet. Space Sci.*, **49**, 1445–1465.

Solomon, S. C., McNutt, R. L., Jr., Watters, T. R., Lawrence, D. J., Feldman, W. C., Head, J. W., Krimigis, S. M., Murchie, S. L., Phillips, R. J., Slavin, J. A., and Zuber, M. T. (2008). Return to Mercury: A global perspective on MESSENGER's first Mercury flyby. *Science*, **321**, 59–62.

Sotin, C., Jaumann, R., Buratti, B. J., Brown, R. H., Clark, R. N., Soderblom, L. A., Baines, K. H., Bellucci, G., Bibring, J.-P., Capaccioni, F., Cerroni, P., Combes, M., Coradini, A., Cruikshank, D. P., Drossart, P. *et al.* (2005). Release of volatiles from a possible cryovolcano from near-infrared imaging of Titan. *Nature*, **435**, 786–789.

Spencer, J. R., Pearl, J. C., Segura, M., Flasar, F. M., Mamoutkine, A., Romani, P., Buratti, B. J., Hendrix, A. R., Spilker, L. J., and Lopes, R. M. C. (2006). Cassini encounters Enceladus: Background and the discovery of a south polar hot spot. *Science*, **311**, 1401–1405.

Spitale, J. and Porco, C. (2007). Association of the jets of Enceladus with the warmest regions on its south-polar fractures. *Science*, **449**, 695–697.

Squyres, S. W. (1980). Volume changes in Ganymede and Callisto and the origin of grooved terrain. *Geophys. Res. Lett.*, **7**, 593–596.

Stofan, E. R., Sharpton, V. L., Schubert, G., Baer, G., Bindschadler, D. L., Janes, D. M., and Squyres, S. W. (1992). Global distribution and characteristics of coronae and related features on Venus: Implications for origin and relation to mantle processes. *J. Geophys. Res.*, **97**, 13 347–13 378.

Stofan, E. R., Smrekar, S. E., Tapper, S. W., Guest, J. E., and Grindrod, P. M. (2001). Preliminary analysis of an expanded corona database for Venus. *Geophys. Res. Lett.*, **28**, 4267–4270.

Strom, R. G. (1984). Mercury. In *The Geology of the Terrestrial Planets*, ed. M. H. Carr. NASA SP-469. Washington, DC: U.S. Government Printing Office, pp. 13–55.

Strom, R. G., Trask, N. J., and Guest, J. E. (1975). Tectonism and volcanism on Mercury. *J. Geophys. Res.*, **80**, 2478–2507.

Strom, R. G., Malhotra, R., Ito, T., Yoshida, F., and Kring, D. A. (2005). The origin of planetary impactors in the inner solar system. *Science*, **309**, 1847–1850.

Tanaka, K. L. (1986). The stratigraphy of Mars. In Proceedings of the 17th Lunar and Planetary Science Conference. *J. Geophys. Res.*, Supplement., pt. 1, **91**, E139-E158.

Tanaka, K. L. (1990). Tectonic history of the Alba Patera-Ceraunius Fossae region of Mars. *Proc. Lunar Planet. Sci. Conf. 20*, 515–523.

Tanaka, K. L. and Davis, P. A. (1988). Tectonic history of the Syria Planum province of Mars. *J. Geophys. Res.*, **93**, 14 893–14 917.

Tanaka, K. L. and Hartmann, W. K. (2008). The planetary timescale. In *The Concise Geologic Time Scale*, eds. J. G. Ogg, G. M. Ogg and F. M. Gradstein. New York: Cambridge University Press, pp. 13–22.

Tanaka, K. L., Golombek, M. P., and Banerdt, W. B. (1991). Reconciling stress and structural histories of the Tharsis region of Mars. *J. Geophys. Res.*, **96**, 15 617–15 633.

Tanaka, K. L., Scott, D.H., and Greeley, R. (1992). Global stratigraphy. In *Mars*, eds. H. H. Kieffer, B. M. Jakosky, C. W. Snyder and M. S. Matthews. Tucson, AZ: University of Arizona Press, pp. 345–382.

Tanaka, K. T., Moore, H. J., Schaber, G. G., Chapman, M. G., Stofan, E. R., Campbell, D. B., Davis, P. A., Guest, J. E., McGill, G. E., Rogers, P. G., Saunders, R. S., and Zimbelman, J. R. (1994). The Venus geologic mappers' handbook. U.S. Geol. Surv. Open-File Rep. 94–438, 66 pp.

Tanaka, K. L., Senske, D. A., Price, M., and Kirk, R. L. (1997). Physiography, geomorphic/geologic mapping, and stratigraphy of Venus. In *Venus II: Geology, Geophysics, Atmosphere, and Solar Wind Environment*, eds. S. W. Bougher, D. M. Hunten and R. J. Phillips. Tucson, AZ: University of Arizona Press, pp. 667–694.

Tanaka, K. L., Dohm, J. M., Lias, J. H., and Hare, T. M. (1998). Erosional valleys in the Thaumasia region of Mars: Hydrothermal and seismic origins. *J. Geophys. Res.*, **103**, 31 407–31 419.

Tanaka, K. L., Skinner Jr., J. A., Hare, T. M., Joyal, T., and Wenker, A. (2003). Resurfacing history of the northern plains of Mars based on geologic mapping of Mars Global Surveyor data. *J. Geophys. Res.*, **108**, doi:10.1029/2002JE001908.

Tera, F., Papanastassiou, D. A., and Wasserburg, G. J. (1974). Isotopic evidence for a terminal lunar cataclysm. *Earth Planet. Sci. Lett.*, **22**, 1–21.

Thomas, P. G. (1997). Are there other tectonics than tidal despinning, global contraction and Caloris-related events on Mercury? A review of questions and problems. *Planet. Space Sci.*, **45**, 3–13.

Thomas, P. G., Masson, P., and Fleitout, L. (1988). Tectonic history of Mercury. In *Mercury*, ed. F. Vilas, C. R. Chapman and M. S. Matthews. Tucson, AZ: University of Arizona Press.

Tuckwell, G. W. and Ghail, R. C. (2003). A 400-km-scale strike-slip zone near the boundary of Thetis Regio, Venus. *Earth Planet. Sci. Lett.*, **211**, 45–45.

Turtle, E. P., Jaeger, W. L., Keszthelyi, L. P., McEwen, A. S., Milazzo, M., Moore, J., Phillips, C. B., Radebaugh, J., Simonelli, D., Chuang, F., and Schuster, P. (2001). Galileo SSI Team, Mountains on Io: High-resolution Galileo observations, initial interpretations, and formation models. *J. Geophys. Res.*, **106**, 33 175–33 200.

Urey, H. C. (1952). *The Planets*. New Haven, CT: Yale University Press.

Watters, T. R. (1988). Wrinkle ridge assemblages on the terrestrial planets. *J. Geophys. Res.*, **93**, 10 236–10 254.

Watters, T. R. (1992). A system of tectonic features common to Earth, Mars, and Venus. *Geology*, **20**, 609–612.

Watters, T. R. (1993). Compressional tectonism on Mars. *J. Geophys. Res.*, **98**, 17 049–17 060.

Watters, T. R. (2004). Elastic dislocation modeling of wrinkle ridges on Mars. *Icarus*, **171**, 284–294.

Watters, T. R. and Maxwell, T. A. (1986). Orientation, relative age, and extent of the Tharsis plateau ridge system. *J. Geophys. Res.*, **91**, 8113–8125.

Watters, T. R., Robinson, M. S., and Cook, A. C. (1998). Topography of lobate scarps on Mercury: New constraints on the planet's contraction. *Geology*, **26**, 991–994.

Watters, T. R., Robinson, M. S., and Cook, A. C. (2001). Large-scale lobate scarps in the southern hemisphere of Mercury. *Planet. Space Sci.*, **49**, 1523–1530.

Watters, T. R., Schultz, R. A., Robinson, M. S., and Cook, A. C. (2002). The mechanical and thermal structure of Mercury's early lithosphere. *Geophys. Res. Lett.*, **29**, 1542.

Watters, T. R., Robinson, M. S., Bina, C. R., and Spudis, P. D. (2004). Thrust faults and the global contraction of Mercury. *Geophys. Res. Lett.*, **31**, doi:10.1029/2003GL019171.

Watters, T. R., Nimmo, F., and Robinson, M. S. (2005). Extensional troughs in the Caloris Basin of Mercury: Evidence of lateral crustal flow. *Geology*, **33**, doi:10.1130/G21678.

Watters, T. R., McGovern, P. J., and Irwin III, R. P. (2007). Hemispheres apart: The crustal dichotomy on Mars. *Annu. Rev. Earth Planet. Sci.*, **35**, 621–652.

Wilhelms, D. E. (1972). Geologic mapping of the second planet. U.S. Geol. Surv. Interagency Report, Astrogeology **55**, 36 pp.

Wilhelms, D. E. (1987). The geologic history of the Moon. U.S. Geol. Surv., Prof. Paper 1348.

Wilhelms, D. E. (1990). Geologic mapping. In *Planetary Mapping*, eds. R. Greeley and R. M. Batson. New York: Cambridge University Press, pp. 208–260.

Wilkins, S. J., Schultz, R. A., Anderson, R. C., Dohm, J. M., and Dawers, N. C. (2002). Deformation rates from faulting at the Tempe Terra extensional province, Mars. *Geophys. Res. Lett.*, **29**, doi:10.1029/2002GL015391.

Wilkins, S. J. and Schultz, R. A. (2003). Cross faults in extensional settings: Stress triggering, displacements localization, and implications for the origin of blunt troughs at Valles Marineris. *J. Geophys. Res.*, **108**, doi:10.1029/2002JE001968.

Wise, D. U., Golombek, M. P., and McGill, G. E. (1979). Tharsis province of Mars: Geologic sequence, geometry, and a deformation mechanism. *Icarus*, **38**, 456–472.

Withers, P. and Neumann, G. A. (2001). Enigmatic northern plains of Mars. *Nature*, **410**, 651.

Wyrick, D., Ferrill, D. A., Morris, A. P., Colton, S. L., and Sims, D. W. (2004). Distribution, morphology, and origins of Martian pit crater chains. *J. Geophys. Res.*, **109**, doi:06010.01029/02004JE002240.

Young, D. A. and Hansen, V. L. (2003). Geologic map of the Rusalka quadrangle (V-25), Venus. U.S. Geol. Surv. Invest. Ser., Map 1-2783, scale 1:5 000 000.

Zahnle, K., Schenk, P., Levison, H., and Dones, L. (2003). Cratering rates in the outer solar system. *Icarus*, **163**, 263–289.

Zuber, M. T., Smith, D. E., Lemoine, F. G., and Neumann, G. A. (1994). The shape and internal structure of the Moon from the Clementine mission. *Science*, **266**, 1839–1843.

Zuber, M. T., Solomon, S. C., Phillips, R. J., Smith, D. E., Tyler, G. L., Aharonson, O., Balmino, G., Banerdt, W. B., Head, J. W., Johnson, C. L., Lemoine, F. G., McGovern, P. J., Neumann, G. A., Rowlands, D. D., and Zhong, S. (2000). Internal structure and early thermal evolution of Mars from Mars Global Surveyor topography and gravity. *Science*, **287**, 1788–1793.